

**Acceptance Studies for ALICE at the Large Hadron Collider:
Analyzing the Effect of Detector Acceptance on hadron— Λ
Angular Correlations, as Part of an Investigation of the
Quark-Gluon Plasma in Small Systems**

by
Ravi Koka

**Undergraduate Thesis
Bachelor in Physics**

**The University of Texas at Austin
May 2024**

Abstract

Acceptance Studies for ALICE at the Large Hadron Collider: Analyzing the Effect of Detector Acceptance on hadron— Λ Angular Correlations, as Part of an Investigation of the Quark-Gluon Plasma in Small Systems

Ravi Koka, BS
The University of Texas at Austin, 2024

SUPERVISOR: Christina Markert

In high energy heavy-ion collisions at the Large Hadron Collider, the temperatures and densities necessary to form the quark-gluon plasma (QGP) are reached. This QGP is a state of matter in which quarks and gluons—ordinarily bound inside color-neutral hadrons—are deconfined. The QGP is believed to have filled the universe microseconds after the Big Bang, when the universe was extremely hot. Strangeness enhancement, an important signature of QGP formation, is observed in p-Pb collisions, calling into question the limits of QGP formation in small systems. To untangle strangeness production in p-Pb, we can utilize two-particle hadron— Λ angular correlations to separate jet-like yields from strangeness production in a possible QGP medium. The yields and widths of these correlations are compared to h—h as a baseline. We evaluate whether these hadron— Λ and h—h correlations are affected by the finite acceptance of ALICE, using 10^7 proton-proton PYTHIA6 monte carlo events at $\sqrt{s} = 7$ TeV. We calculate the yields and widths corresponding to the near- and away-side peak of our hadron— Λ and h—h correlations across various kinematic cuts, and calculate the corresponding ratios (hadron— Λ over h—h). We

find agreement between the yields and yield ratios across all acceptances. In addition, we find a broad agreement in the widths of the correlations, and no deviations in the width ratios. This suggests our $h-\Lambda$ and $h-h$ correlations require no extra systematic corrections due to finite acceptance. The code used for this analysis is available at <https://github.com/ravikoka/broad>

Table of Contents

Chapter 1: Introduction	7
1.1 A Crash Course in Particle Physics	7
1.1.1 The Standard Model	7
1.1.2 Quantum Chromodynamics	9
1.1.3 Hadrons! Hadrons! Hadrons!	10
1.1.4 Relativistic Kinematics	12
1.1.5 Cross Sections	14
1.1.6 Feynman Diagrams	17
1.1.7 Understanding Hadronization and Jets	18
1.2 The Quark-Gluon Plasma	20
1.3 The Anatomy of a Heavy-Ion Collision	22
1.3.1 The Origins of Strangeness Enhancement	24
1.4 A Large Ion Collider Experiment (ALICE)	27
1.4.1 Inner Tracking System (ITS)	29
1.4.2 Time Projection Chamber (TPC)	30
1.4.3 Time-of-Flight (TOF)	33
1.4.4 Calorimetry	34
1.4.5 VZERO	36
Chapter 2: Motivations & Methods	37
2.1 Prelude	37
2.2 A Brief Word on Histogramming	37
2.3 Hadron— Λ Angular Correlations	40
2.4 PYTHIA	44
2.5 Motivation	45
2.6 Analysis Description	46
2.7 Fitting Procedure	48
Chapter 3: Results & Discussion	56
3.1 Generated Distributions	56
3.2 Yields	58
3.3 Widths	59
3.4 Evaluation of Fit Stability	60
3.5 Future Work	63

Chapter 4: Summary	64
Chapter 5: Resources for the Aspiring Undergraduate Researcher	65
Appendix A: Fits	67
A.1 Double Gaussian	67
A.2 Double Generalized Gaussian	69
A.3 Double Von Mises	71
Appendix B: Dense Yield Ratios	73
Works Cited	74

Chapter 1: Introduction

Knees weak, ions are heavy.

- Unknown

1.1 A Crash Course in Particle Physics

1.1.1 The Standard Model

Given our current understanding of the universe, there are four fundamental forces governing the interactions between all known particles:

- Strong Force: The strongest interaction, describing the dynamics of quarks and gluons. This interaction is described by quantum chromodynamics. The strong force is relevant on length scales within a proton or neutron.
- Electromagnetism: Responsible for electricity and magnetism, describing photons and particles that carry electric charge.
- Weak Force: Responsible for nuclear decays. This is the only interaction that can change flavor. The weak force is also the only interaction that is not symmetric under parity.
- Gravity: Describes the gravitational force, relevant from human to cosmological scales in spacetime.

The *Standard Model* describes the strong force, electromagnetism, and the weak force. This is the arena of particle and nuclear physics. Our best description of gravity comes from *general relativity*, which describes spacetime on the largest scales by endowing it with a metric field. Since the effects of gravity are only measurable on large scales, it is not relevant at the small scales probed at our current colliders, and will not be expanded upon in this thesis.

The underlying framework behind the Standard Model is quantum field theory. In a hand-wavy sense, to each type of particle we associate a field; particles are excitations in these fields (ie. an electron is an excitation in the electron field). Whether two given fields are coupled determines whether they can interact. The Standard Model is an effective field theory, so we can write down a Lagrangian density for it, from which, in principle, we can derive the dynamics for a given system. In practice, this is extremely difficult.

One way of conceptualizing particle interactions via the Standard Model is through the exchange of gauge bosons. For example, the photon mediates electromagnetism, while the gluon mediates the strong force. Whether a particle feels a force depends on if it carries the charge of the force. Quarks are the only fundamental particles that participate in the strong interaction because they carry *color charge*, while all other massive particles—the leptons—do not carry this charge. A basic diagram of the Standard Model particles is shown in Fig. 1.1.

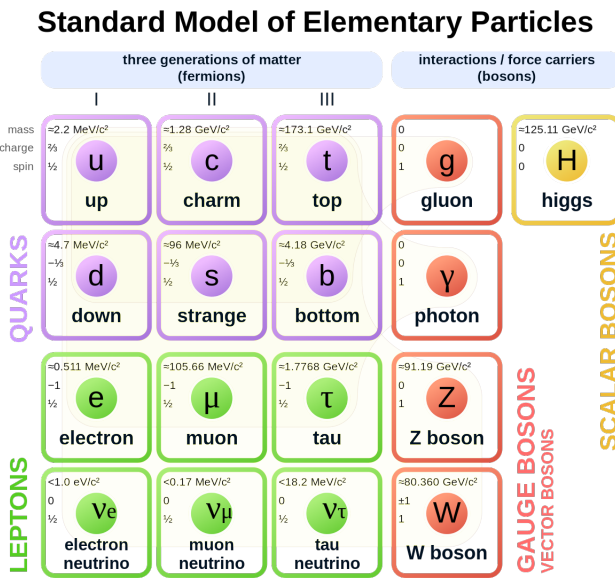


Figure 1.1: The Standard Model of particle physics. From: *Wikipedia*.

1.1.2 Quantum Chromodynamics

Quantum chromodynamics (QCD), also known as the strong force or color force, describes the dynamics between quarks and gluons. The name comes from the fact that there are three types of charge, known as color charge: red, green, and blue. This theory is incredibly complicated because unlike with photons and electromagnetism, the carriers of the strong force—the gluons—carry the charge of the interaction. There are eight types of gluon, corresponding to different color states. This makes calculations in QCD particularly challenging. In addition, there are two unusual features of QCD, known as asymptotic freedom and color confinement.

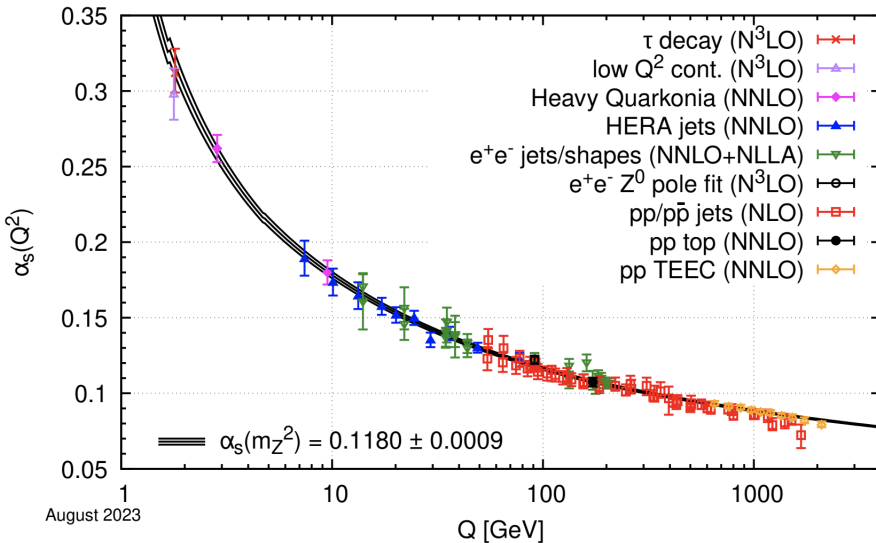


Figure 1.2: A plot of α_s across various energy scales. As the energy scale increases, the coupling constant decreases asymptotically [1].

In quantum field theory, a common method to make headway on a problem is to utilize perturbation theory. This is only possible if the coupling constant associated with the interaction is less than one, however this is often not true in the case of the strong force. This makes understanding QCD extremely difficult. However, as the energy scale of the problem increases (or the length scale decreases), the value of the strong coupling constant α_s decreases (Fig. 1.2). We call this phenomenon asymptotic freedom, for which the 2004

Nobel Prize in Physics was awarded to David Gross, Frank Wilczek, and David Politzer. In this regime, we can utilize perturbative QCD (pQCD) to solve problems.

If we take a $q\bar{q}$ bound state and try to separate the pair, we have to put so much energy in that we simply create two new $q\bar{q}$ pairs. The important consequence is that we will never observe a lone quark. We can model this potential as a linear one for large separations:

$$V(r) = \frac{-4\alpha_s}{3} \frac{1}{r} + \sigma r + c \quad (1.1)$$

where r is the separation between the quarks, σ is a constant that acts like a string tension, and c is a constant. This effective model of color confinement is expanded on in Section 2.4.

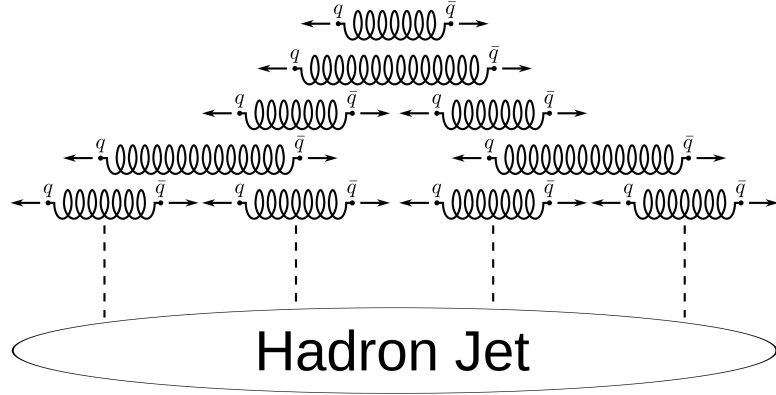


Figure 1.3: A depiction of how a jet is formed. In collider physics, scatterings between partons that involve high momentum transfer can produce two outgoing high-momentum partons. In this example, a $q\bar{q}$ pair is produced. As the original $q\bar{q}$ pair separates, new pairs are formed. This is due to color confinement.

1.1.3 Hadrons! Hadrons! Hadrons!

Due to color confinement, we will never observe lone partons (quarks and gluons). Instead, we only see color-neutral bound states called *hadrons*. For a meson, a hadron consisting of two quarks, this can be accomplished by having a quark and anti-quark with

opposite color charge. For a baryon, consisting of three quarks¹, we would have a red, green, and blue quark (or anti-red, anti-green, and anti-red) which adds up to white (color-neutral). Note, when we count quarks in hadrons, we are referring to the valence quarks which is a simplification. Hadrons like the proton are actually extremely dynamic, with $q-q\bar{q}$ pairs popping in-and-out of existence while gluons whiz about—this is known as the quark sea.

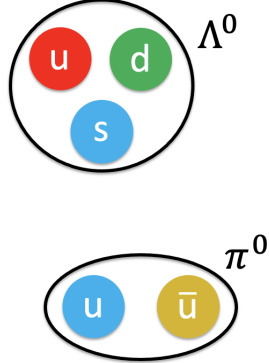


Figure 1.4: An example of two hadrons. Importantly, the color charge adds to color-neutral in each case. The Λ^0 is relevant to this analysis.

The lifetime of a hadron is related to the interaction that mediates its decay, as demonstrated in Fig. 1.5. Strong decays lead to the shortest lifetimes ($\sim \text{fm}/c$). At hadron colliders, we only detect the final-state hadrons that reach our detector. To study the underlying partonic dynamics, we must work up the chain, reconstructing decays from the final-state particles. Remarkably, the proton is the only stable hadron, with a lifetime constrained above 10^{34} years (the universe is 13×10^9 years old). If we measure proton decay, this could indicate a possible grand unified theory.

¹Technically, a meson consists of an even number of quarks and a baryon consists of an odd number. In reality, a meson with more than 2 quarks and a baryon with more than 3 are extremely rare.

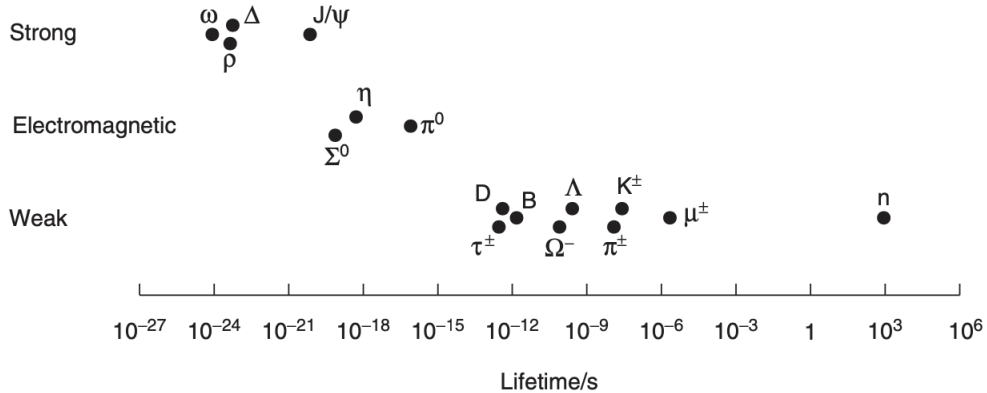


Figure 1.5: A rough plot of hadrons arranged by their lifetime and type of decay [2].

1.1.4 Relativistic Kinematics

At the Large Hadron Collider, particles are accelerated to nearly the speed of light before they collide. This is solidly in the regime of special relativity, where time and space blend into a unified spacetime. Typically, we define a right-handed coordinate system with z along the beamline, as shown in Fig. 1.6.

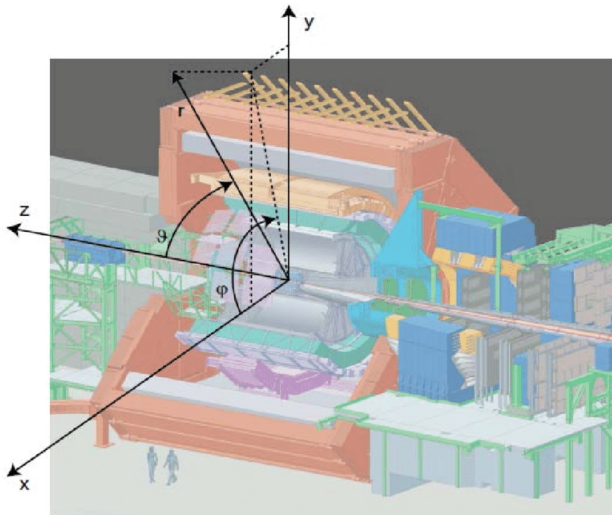


Figure 1.6: The ALICE coordinate system is a right-handed coordinate system with z aligned along the beam. The transverse plane, or the $x-y$ plane, is perpendicular to the z -axis. The longitudinal direction and z -axis are synonymous.

Denote the lab frame as the unbarred frame. Let us consider an inertial frame that moves with velocity v_z in the z direction, representing a particle whose rest frame we denote as the barred frame. We can transform four-vectors from the lab frame to the particle's frame using the Lorentz transformation:

$$x^{\bar{\mu}} = \sum_{\nu=0}^3 \Lambda^{\bar{\mu}}{}_\nu x^\nu \quad (1.2)$$

where $\bar{\mu}$ runs from 0 to 3. Explicitly, the Lorentz transformation can be written as a matrix:

$$\Lambda^{\bar{\mu}}{}_\nu = \begin{pmatrix} \cosh y & 0 & 0 & -\sinh y \\ 0 & 1 & 0 & 0 \\ 0 & 0 & 1 & 0 \\ -\sinh y & 0 & 0 & \cosh y \end{pmatrix} \quad (1.3)$$

where $y = \tanh^{-1} v$ is the boost parameter, also known as the rapidity. Since we are boosting into a frame that moves with v_z along the z -axis:

$$y = \tanh^{-1} v_z = \tanh^{-1} \frac{\gamma m v_z}{\gamma m} \quad (1.4)$$

$$= \tanh^{-1} \frac{p_z}{E} \quad (1.5)$$

$$= \frac{1}{2} \ln \frac{1 + \frac{p_z}{E}}{1 - \frac{p_z}{E}} \quad (1.6)$$

$$= \frac{1}{2} \ln \frac{E + p_z}{E - p_z} \quad (1.7)$$

This is the familiar expression for rapidity used in collider physics. For a high momentum particle with most of its momentum in the $x-y$ plane, $p_z \approx 0$ so $y \approx 0$. For a high momentum particle with most of its momentum in the z direction, $E \approx p_z$ and, in the limit, $y \rightarrow \infty$. Similarly, if most of the momentum is in the $-z$ direction, then $y \rightarrow -\infty$. Thus, for relativistic particles, rapidity is related to the angle of emission from the beam axis. We use rapidity instead of θ because differences in rapidity are Lorentz invariant. Thus, when

boosting between the lab frame and center-of-mass frame, y distributions are merely shifted, not distorted.

To see this fact, consider three inertial frame A , B , and C . To boost from A to C , we could boost from A to B and then from B to C . This is equivalent to simply adding the rapidities when used as the boost parameter:

$$\Lambda(y_{AC}) = \Lambda(y_{AB})\Lambda(y_{BC}) = \Lambda(y_{AB} + y_{BC}) \quad (1.8)$$

Thus,

$$y_{AC} = y_{AB} + y_{BC} \quad (1.9)$$

Since rapidity is related to the angle of emission of a relativistic particle from the beam line, it is convenient to define pseudorapidity, η :

$$\eta \equiv \frac{1}{2} \ln \frac{|\mathbf{p}| + p_z}{|\mathbf{p}| - p_z} = -\ln \left[\tan \left(\frac{\theta}{2} \right) \right] \quad (1.10)$$

Pseudorapidity can be explicitly written in terms of the angle from the beam axis, and for relativistic particles $m \ll |\mathbf{p}| \implies E \approx p$, so $y \approx \eta$. Since pseudorapidity is directly related to the angle of emission and differences in pseudorapidity are approximately Lorentz invariant, we use η instead of rapidity. We refer to η values near 0 as midrapidity and values far from 0 as forward rapidities.

1.1.5 Cross Sections

Scattering is the heart of experimental particle physics. If we want to know the structure of some substance, we can scatter particles off of it, see what comes out, and reconstruct what happened. This is how the famed Rutherford gold foil experiment determined atomic nuclei exist. This is also how deep inelastic scattering demonstrated there are three point-like particles—valence quarks—in the proton. Even in other areas of physics, scattering

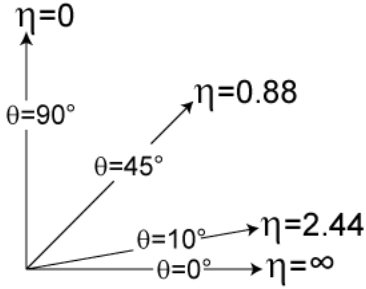


Figure 1.7: A diagram demonstrating how pseudorapidity relates to θ , the angle from the beamline. Source: *Wikipedia*.

experiments are ubiquitous. For example, electron microscopes scatter a beam of electrons off a target to resolve an image.² If we are being slightly facetious, then we can even say a microscope scatters light off a target, recollecting that scattered light into your eye to make an image.

To quantitatively understand scattering, let's consider a fixed-target experiment, where we shoot a beam of particle species 1 at a stationary target consisting of particle species 2. We can characterize this experiment by how often an interaction happens. The higher the flux of the incident beam, the higher the rate of interaction per particle species 2. We can thus write:

$$R_2 = \sigma\phi_1 \quad (1.11)$$

where σ is the *cross section*, a constant of proportionality with dimensions of area. We can conceptualize σ as the effective area of each target particle, but this is rarely actually true. The cross section characterizes the probability of a given interaction, abstracting away the underlying quantum mechanics.

In experiments like deep inelastic scattering or the Rutherford experiment, a beam of particles is scattered off of a target, and the angular distribution of the scattered particles

²In a sense, this makes Electron-Ion Collider the world's soon-to-be largest electron microscope.

gives information about the structure of the target. To capture this angular information, it's useful to work with the differential cross section $d\sigma/d\Omega$, where:

$$\sigma = \int \frac{d\sigma}{d\Omega} d\Omega \quad (1.12)$$

In short, the differential cross section is the rate per target particle of incident particles scattered into a certain solid angle, divided by the incident flux. This cross section is a function of both θ and φ , but often symmetry in φ allows us to reduce the differential cross section to a function of just θ .

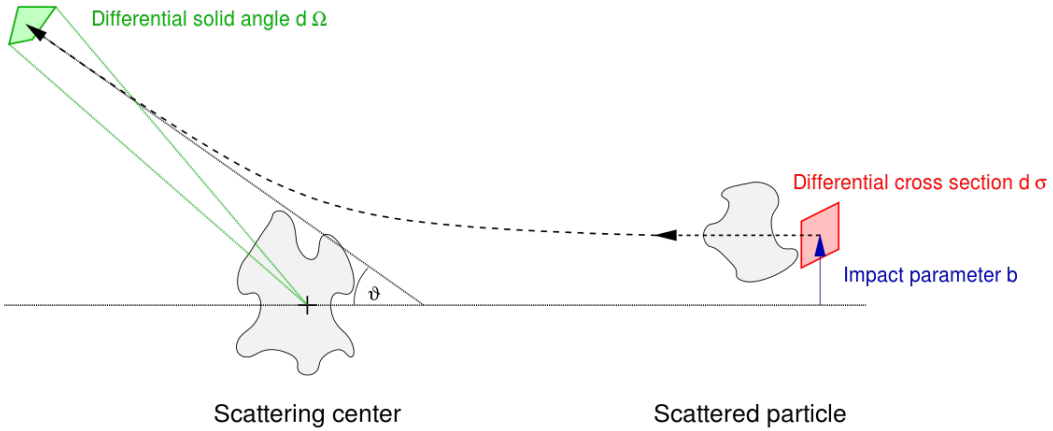


Figure 1.8: The set-up of a standard scattering problem. A particle originally parallel to the z -axis scatters off a target, leaving at an angle ϑ . This angle is called the scattering angle. The differential cross section gives the probability a particle passing through an area $d\sigma$ is scattered into some solid angle $d\Omega$. Source: *Wikipedia*.

As an example of a differential cross section, let us consider scattering in a Coulomb potential—the *only* potential where the cross section obtained from quantum and classical calculations agree. Let $Z_1 e$ be the charge a particle incident on a second particle of charge $Z_2 e$, where e is the elementary charge. If the incident particle has initial velocity v_0 , this differential cross section, also known as the Rutherford cross section, is then given by:

$$\frac{d\sigma}{d\Omega}(\vartheta) = \left(\frac{Z_1 Z_2 e^2}{8\pi\epsilon_0 m v_0^2} \right)^2 \csc^4(\vartheta/2) \quad (1.13)$$

This represents the angular distribution of scattered particles. Philosophically, the differential cross section tells us how the final state distribution of particles relates to the initial state. Often, the initial state represents particles fired along the z -axis, and the final state is the angular distribution of scattered particles. However, differential cross sections are not restricted to angular distributions. One can also define cross sections in terms of E or other kinematic variables:

$$\frac{d\sigma}{dE} \tag{1.14}$$

or define two-dimensional differential cross sections:

$$\frac{d^2\sigma}{dEd\eta} \tag{1.15}$$

1.1.6 Feynman Diagrams

Feynman diagrams are an important calculational tool in particle physics, representing the transition between two quantum states. In fact, these pictorial representations actually allow us to work out the probability of a given interaction. Consider the diagram in Fig. 1.9, representing the $2 \rightarrow 2$ process $a + b \rightarrow c + d$. By this notation, we mean we start in a state consisting of particles a and b , ending in a state consisting of particles c and d . The leftmost diagram depicts how the initial and final states are related by the exchange of the boson X . This diagram actually represents two possible time-orderings of the process, which becomes relevant when we need to actually calculate interaction probabilities. From quantum field theory, we can cook up rules for calculating from these diagrams, and a given process generally has an infinite number of associated diagrams. If the coupling constant for a given interaction is small (eg. electromagnetism where $\alpha \approx 1/137$) then we need only consider the highest order diagrams. Unfortunately, in the case of QCD where $\alpha_s \approx 1$ unless we are at high energy scales, this makes calculations intractable. In a sense, collider experiments measure final state particles to reconstruct the original process represented by these Feynman diagrams.

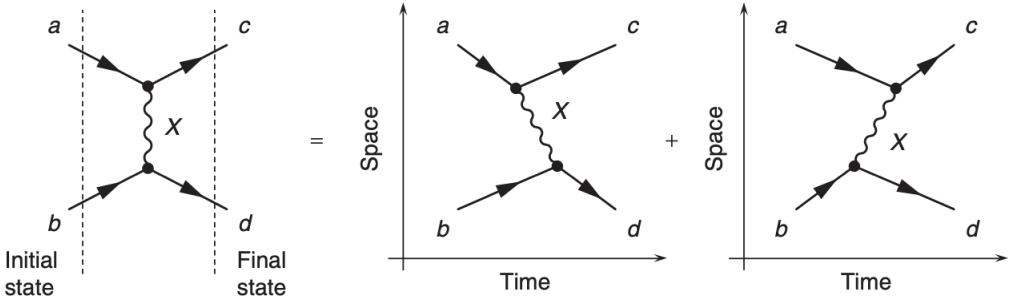


Figure 1.9: A depiction of Feynman diagrams for the general process $a + b \rightarrow c + d$, mediated by a gauge boson X . The leftmost diagram that summarizes the interaction actually represents two possible time-orderings [2].

1.1.7 Understanding Hadronization and Jets

Due to color confinement, we will never observe a lone quark. At some point, the partons in a given high energy interaction must undergo hadronization, the formation of color-neutral bound states. Since hadronization is non-perturbative, we must resort to models to understand the process. Let's examine a common model of hadronization—the *Lund string model*—in the context of the simple $2 \rightarrow 2$ process $e^+e^- \rightarrow q\bar{q}$, with the associated Feynman diagram shown in Fig. 1.10. In the Lund string model, the two quarks produced in the interaction are initially free and move apart with high relative velocity. A color flux tube, also called a string, connects the two quarks, representing energy in the color field between the pair. The force across the tube is assumed constant, like tension in a string, which gives rise to a linear potential in the separation (Eq. 1.1). As the quarks separate, energy is transferred from the partons to the color flux tube until it is energetically favorable for the tube to snap and two pairs of quarks connected by smaller tubes form. We can imagine this like stretching an elastic string until it reaches the yield point and breaks. The smaller strings that connect the two new pairs of partons continue to fragment further and further, producing two clusters of hadrons that each move in the direction of the original quarks. Each cluster of hadrons is called a jet, which we measure in a detector. A cartoon of this process is depicted in Fig. 1.3. Thus, jets of hadrons give us information about the underlying partonic processes.

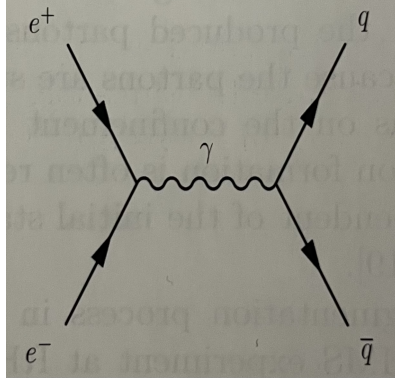


Figure 1.10: A simple Feynman diagram describing $e^+e^- \rightarrow q\bar{q}$, taken from [3].

To quantify how hadrons are produced from partonic scattering, we utilize *fragmentation functions*. Consider the $2 \rightarrow 2$ scattering $e^+e^- \rightarrow q\bar{q}$. The quark fragments into a hadron h which is observed in the detector. If we denote the center-of-mass energy as Q , then in the center-of-mass frame each beam has energy $Q/2$. Due to momentum conservation, the quark and anti-quark are produced in opposite directions, and each carry energy $Q/2$. We can thus define z , the energy the final-state hadron carries E_h over the fraction of energy the quark initially had:

$$z = \frac{2E_h}{Q} \quad (1.16)$$

Which allows us to define a differential cross-section as a function of z [3]:

$$\frac{d\sigma(e^+e^- \rightarrow hX)}{dz} = \sum_q \sigma(e^+e^- \rightarrow q\bar{q}) [D_q^h(z) + D_{\bar{q}}^h(z)] \quad (1.17)$$

where q is a sum over quark flavors and σ is a cross section related to the underlying partonic process. Here D_q^h is the fragmentation function which represents the probability of producing a final-state hadron with momentum fraction z . Importantly, fragmentation functions are assumed universal—*intrinsic* to a certain process. Thus, fragmentation functions measured from e^+e^- collisions should also apply to pp collisions. This example is analogous

to the initial hard scatterings in a heavy-ion collision where two back-to-back partons are produced which hadronize into a dijet (two back-to-back jets).

Fragmentation functions are reminiscent of *parton distribution functions* which give the probability of observing a quark within a hadron as a function of the momentum fraction of the quark. At hadron colliders, a description of hadronization is much more difficult. To accurately calculate cross-sections, we need to consider higher order diagrams and utilize parton distribution functions. In order to make progress, we rely on factorization theorems which separate partonic cross sections (calculable in pQCD), fragmentation functions, and parton distribution functions.

1.2 The Quark-Gluon Plasma

The overarching goal of heavy-ion physics is to elucidate the properties of the quark-gluon plasma (QGP), a state of matter that existed in the first microseconds after the Big Bang (Fig. 1.11). This represents one patch on the QCD phase diagram (Fig. 1.12), which maps states of QCD matter for various temperatures and baryon chemical potentials (loosely, density). In this state, the quarks and gluons that are ordinarily locked inside hadrons are deconfined. Thus, by probing the QGP, we can begin to understand the partonic degrees of freedom in QCD while assembling a picture of the early universe. This earns the QGP its nickname as the "primordial soup."

In high energy heavy-ion collisions at the Large Hadron Collider, we produce the necessary conditions to deconfine the quarks and gluons that make up nucleons, leading to the creation of mini QGPs. By studying the final state particles our detectors measure, we can infer the dynamics of these high energy collisions and the QGP. Interestingly, the QGP is a strongly interacting liquid with a tiny shear viscosity to entropy ratio that pushes the limit of what physicists believe is possible [4]. This makes the QGP the most perfect liquid ever created. Another unexpected discovery was that the transition from quark-gluon plasma to hadron gas is smooth, rather than a discontinuous cross-over. The critical temperature of the QGP is typically taken as $T_c \approx 160$ MeV (around 10^5 times hotter than the center of

the Sun).

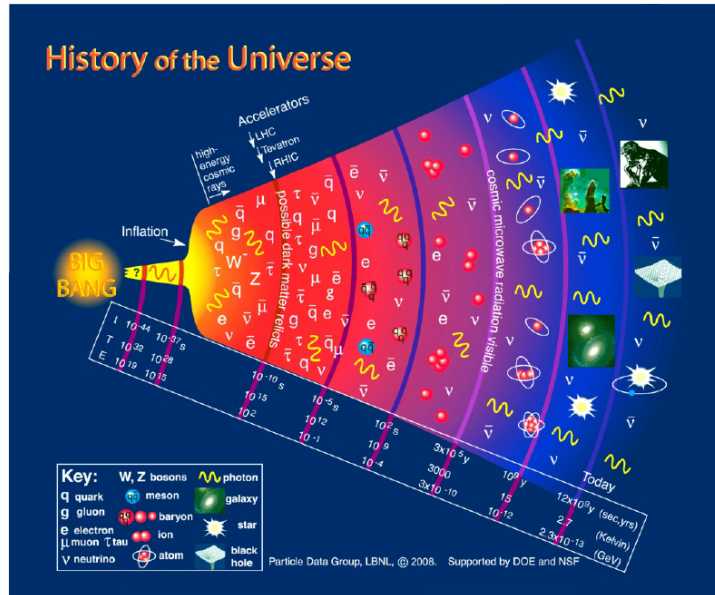


Figure 1.11: A diagram of the history of the universe, from the perspective of a particle physicist. The outline of the diagram roughly corresponds to the scale factor which quantifies the expansion of the universe. Source: Particle Data Group.

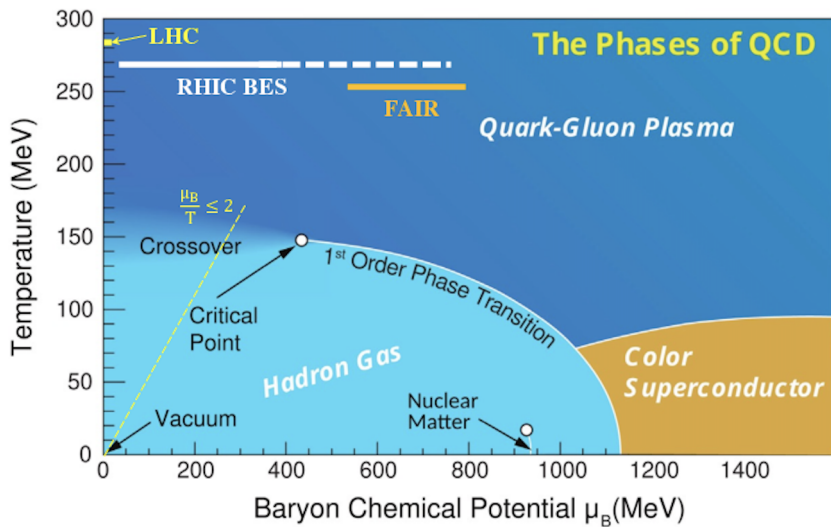


Figure 1.12: A basic depiction of the QCD phase diagram, the main object of study in relativistic heavy-ion physics [5]. This diagram is rich unexplored territory and physics.

1.3 The Anatomy of a Heavy-Ion Collision

The spacetime structure of a heavy-ion collision is presented in Fig. 1.13. The hyperbolae represent lines of constant proper time, an inherent part of Minkowski space. In a relativistic heavy-ion collision, two Lorentz contracted nuclei smack into each other. During the initial stages, certain partons may *hard scatter*, an interaction characterized by large four-momentum exchange. This hard scatter produces jets of hadrons that can reach our detector. After some time, a QGP droplet forms and undergoes hydrodynamic expansion. Next, hadronization begins as the deconfined partons form hadrons. Eventually, inelastic collisions cease and particle abundances are frozen (chemical freeze-out), and elastic scattering ceases, freezing momentum distributions (kinetic freeze-out). The final-state particles then free-stream into the detector where they are measured. The time it takes from the initial hard-scatterings to freeze-out is on the order of $10 \text{ fm}/c$ or 10^{-22} s .

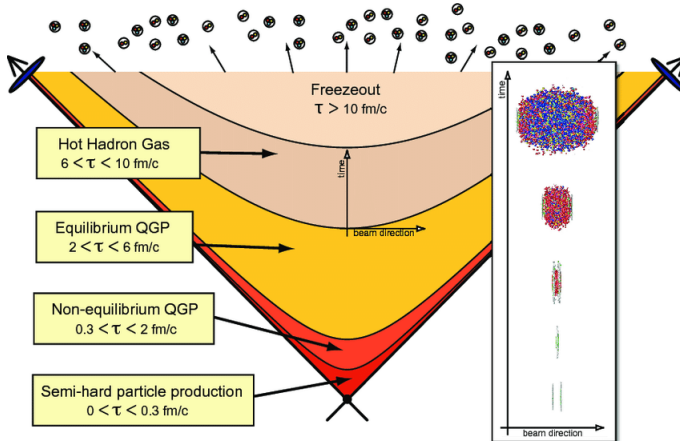


Figure 1.13: The spacetime structure of a heavy-ion collision. The y -axis represents a spatial coordinate and the x -axis represents time [6]. The hyperbolae correspond to curves of constant proper time.

We often characterize heavy-ion collisions by centrality. This is related to the impact parameter b of the collision, which is depicted in Fig. 1.14. The nucleons that participate in the collision are called participants while those that do not are called spectators. A more central collision corresponds to a low value of impact parameter, thus a higher particle multiplicity and a larger QGP. A less central, or peripheral, collision means a larger impact

parameter, leading to lower multiplicities and a smaller QGP. In other words, the region of overlap between the colliding nuclei is larger for more central collisions. This basic notion of centrality and multiplicity will become relevant in our discussion of strangeness enhancement.

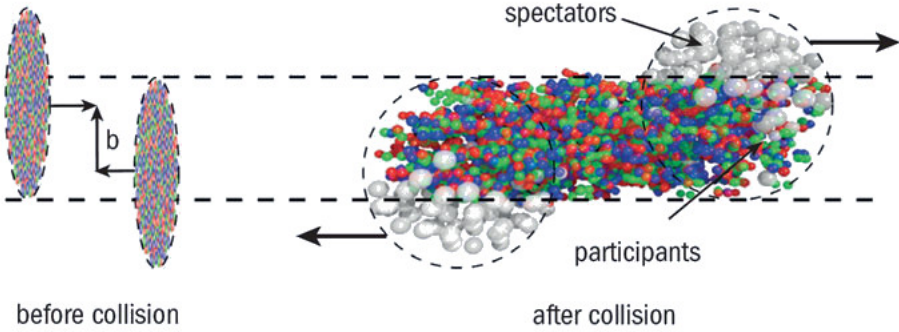


Figure 1.14: The basic picture of a heavy-ion collision [7]. Nucleons that experience a collision are called participants, while those that do not are called spectators. These spectators are assumed to fly off in a straight path. Nucleons that suffer an inelastic collision are called wounded nucleons.

1.3.0.1 QGP Signatures & Small Systems

There are many signatures of QGP formation in heavy-ion collisions, including, but not limited to:

1. Jet Quenching: partons that eventually form the hadrons of a jet experience collisional energy loss and radiative energy loss in the QGP, much like bremsstrahlung radiation.
2. Flow: the hydrodynamic flow in the QGP leads imprints itself in correlations of final-state particles.
3. Strangeness Enhancement: strange quark production increases relative to up and down quark production.

We mention these signatures because of their relevance to correlation analyses, the topic of this thesis. While QGP formation in Pb-Pb collisions was not a surprise, smaller

systems such as p-Pb and p-p show collective effects and strangeness enhancement that indicate the creation of QGP droplets. In fact, p-p is often taken as a reference to Pb-Pb data, serving as a normalization that allows us to interpret results from heavy-ion collisions [8]. In addition, p-Pb is utilized to disentangle cold nuclear matter effects. If a medium is indeed formed in these smaller systems, then it calls into question our understanding of the QGP. To date, jet quenching has not been observed in p-p or p-A collisions, and light-ion runs are needed to gauge the expected magnitude of jet quenching in small systems [9]. Determining whether a medium is created in small system, in essence, the limits of QGP formation, is the underlying motivation behind this thesis.

1.3.1 The Origins of Strangeness Enhancement

The ordinary protons and neutrons that make up the baryonic matter we interact with contain only up and down valence quarks³. At the Large Hadron Colliders, we can access energies required to produce strange and anti-strange quarks. For a given hadron, the net strangeness is defined as:

$$S = -(n_s - n_{\bar{s}}) \quad (1.18)$$

where n_s is the number of strange quarks and $n_{\bar{s}}$ is the number of anti-strange quarks. Note that a strange quark has $S = -1$. The minus sign is an arbitrary choice to match the sign of the electric charge. To leading order, there are 4 diagrams that describe strangeness production. Since flavor is conserved, any strangeness we observe must originate from an $s\bar{s}$ pair.⁴ As suggested by Rafelski and Müller in 1982, it turns out that enhanced strangeness production in heavy-ion collisions could signify the creation of a QGP [10]. This occurs because gluon fusion (the top left diagram in Fig. 1.15) can occur faster than $q\bar{q} \rightarrow s\bar{s}$.

³We are ignoring a discussion of the quark sea.

⁴However, there must be some process that admits matter-antimatter asymmetry in the early universe, otherwise we wouldn't be here!

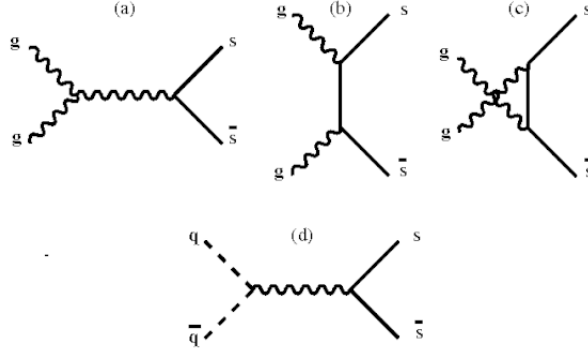


Figure 1.15: Leading order diagrams for strangeness production. Source: *Wikipedia*.

The enhancement of strangeness production can be quantified with the Wroblewski ratio:

$$\lambda_s = \frac{2\langle s\bar{s} \rangle}{\langle u\bar{u} \rangle + \langle d\bar{d} \rangle} \quad (1.19)$$

Thus, we can calculate this ratio as a function of multiplicity (system or medium size). If we see an increase from "small systems" like p-p and p-Pb to Pb-Pb, we've found a signature of QGP formation. This strangeness enhancement has been observed and is shown in Fig. 1.16. Strangeness enhancement seems to saturate as multiplicity increases. Interestingly, high multiplicity p-Pb collisions feature strangeness enhancement that overlaps with low multiplicity Pb-Pb collisions. This suggests possible QGP formation in p-Pb, which is related to the idea of medium formation in small systems. Thus, by understanding the mechanism behind strangeness enhancement in p-Pb, we can begin to determine whether we are creating a QGP in small systems.

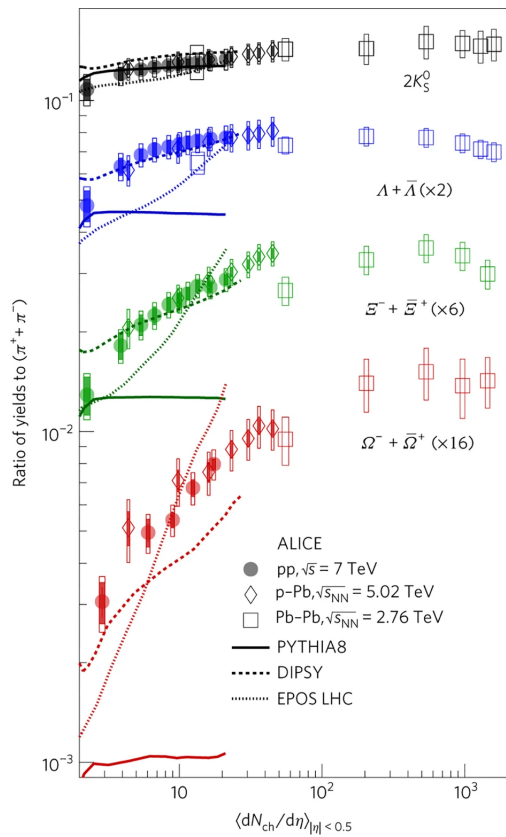


Figure 1.16: ALICE data demonstrating strangeness enhancement. The horizontal axis represents multiplicity.

1.4 A Large Ion Collider Experiment (ALICE)

The Large Hadron Collider is the world's premier hadron collider, capable of accelerating protons and lead ions to near luminal speeds. This allows physicists to probe the interactions between fundamental particles, exploring the implications of the Standard Model and searching for new physics. The collision systems and energies⁵ at the LHC are:

System	Energy
Proton-Proton (p-p)	$\sqrt{s} = 13.6 \text{ TeV}$
Proton-Lead (p-Pb)	$\sqrt{s_{NN}} = 8.16 \text{ TeV}$
Lead-Lead (Pb-Pb)	$\sqrt{s_{NN}} = 5.36 \text{ TeV}$

Note that these energies are tiny. The average housefly has a maximum speed of around 2.3 ms^{-1} and an average mass of 12 mg. Thus, a fly has almost 14,000 times the kinetic energy in a p-p collision. The key is the Large Hadron Collider is capable of creating systems with incredible energy density; individual protons are much smaller than a fly.

At the LHC, there are two beamlines that cross at four *interaction points*. These interaction points are the locations of the LHC's major experiments: ATLAS, ALICE, CMS, and LHCb. Each beamline carries bunches of protons or lead ions, that pass through each other at the interaction points—a bunch crossing. This produces the collisions we seek to untangle but also a background in the form of pile-up.

The ALICE experiment at the LHC is a dedicated experiment for relativistic heavy-ion physics, specializing in the identification and characterization of low-momentum particles. ALICE weighs approximately 10,000 metric tons and has dimensions of $16 \times 16 \times 26 \text{ m}^3$ [11]. By using various layers of detectors, ALICE obtains the kinematic information that becomes the backbone of analyses. At the heart of particle detection and measurement is the concept of a *track*, a path a particle takes in the detector as it travels through the various components. For reasons given in Section 1.4.2, a large magnetic field is maintained in the inner barrel of the ALICE detector, causing charged particle to create curved tracks. Identifying these

⁵If you're curious why we use \sqrt{s} for the center-of-mass energy, read up on Mandelstam variables.

tracks is a challenge, especially with the high multiplicities of heavy-ion collisions, meaning a high track density. Tracing the path of a particle through multiple complicated detectors requires extraordinary synchronization of many components. Below, we touch on the basics of particle identification and measurement.

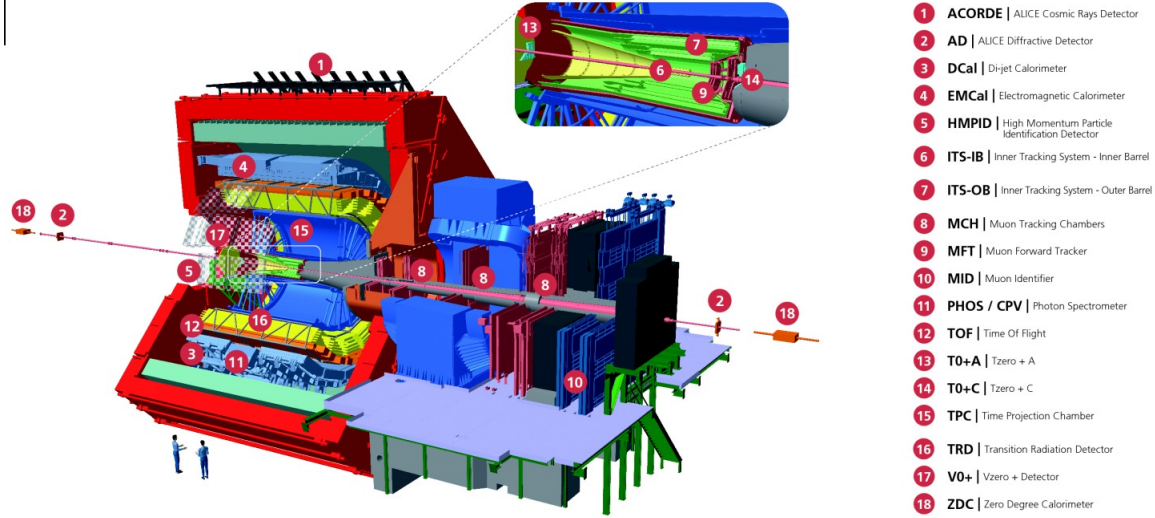


Figure 1.17: A schematic of the ALICE experiment during Run 3 [12]. The proceeding sections will follow the path a particle takes through the various detectors.

Often, it is useful to define a *separation power* that quantifies our ability to discriminate between two different types of particles. Given a detector resolution of σ , this separation power is given by [2]:

$$n_\sigma = \frac{R_A - R_B}{\sigma} \quad (1.20)$$

where R_A is the average response of the detector to particle species A and R_B is the average response to particle species B . As σ increases, the separation power decreases, corresponding to a poor ability to discriminate. A large difference in response enables a better ability to discriminate. To ensure the quality of tracks, one might exclude tracks with small n_σ .

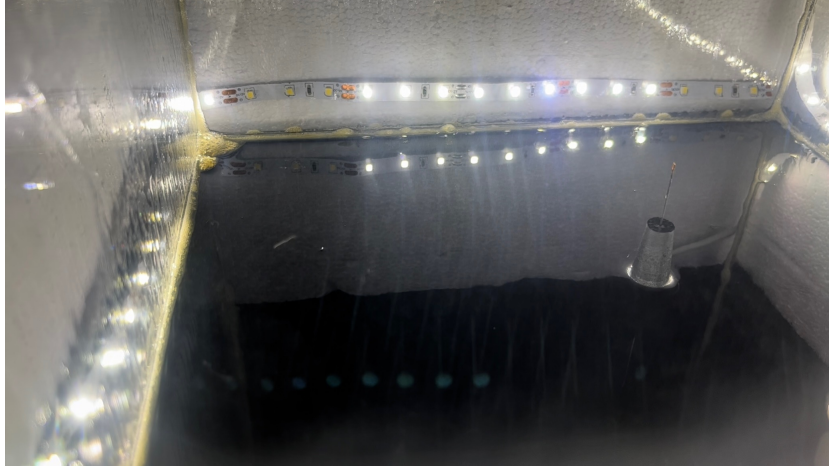


Figure 1.18: A cloud chamber built by the author of this thesis and another University of Texas undergraduate. The small white streak towards the left of the photo is an alpha track, produced when a helium nucleus causes supersaturated alcohol at the bottom of the chamber to condense. The concept of a track has its roots in early cloud and bubble chambers used to unravel the particle zoo.

1.4.1 Inner Tracking System (ITS)

The inner tracking system (ITS) is the closest detector to the beamline, consisting of 6 layers of silicon detectors with an overall pseudorapidity coverage of $|\eta| \leq 0.9$ [11]. These silicon detectors are capable of dealing with high track density near the beamline, which is vital for heavy-ion collisions. In particular, the ITS is used to locate the primary vertex, the initial collision point, and secondary vertices, the location of weak decays that occur after the initial collision (eg. the decays of hyperons or B mesons). The 4 outermost layers of the ITS read out an analog signal which is used for particle identification via the Bethe-Bloch equation for dE/dx , explained in the next section [11]. The innermost layers simply register hits. The ITS has good spatial resolution for particles and tracks.

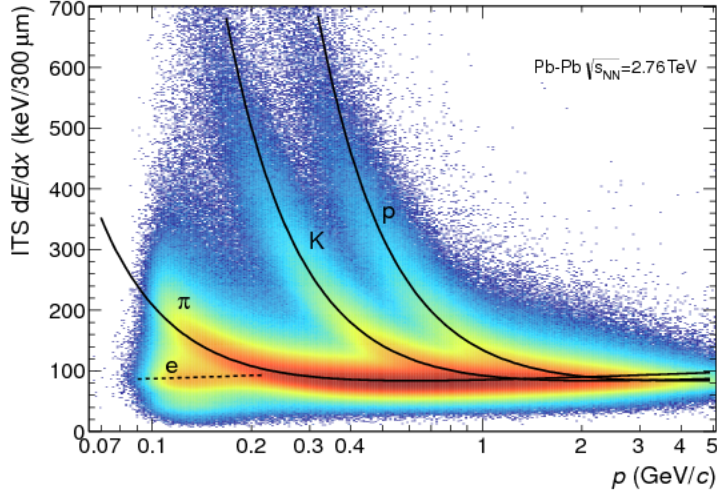


Figure 1.19: dE/dx curves of particles in the ITS. The ITS measures both dE/dx and p [13].

1.4.2 Time Projection Chamber (TPC)

The ALICE time projection chamber (TPC)⁶ is a large volume filled with gas, used for particle identification and tracking with pseudorapidity coverage of $|\eta| < 0.9$. When a charged particle passes through, it ionizes the gas. The ionization electrons then drift along the z axis due to an applied electric field and are measured when they reach the end-plates. A measurement of the drift time gives a location in z . Where the electron deposits on the end-plates gives the x - y coordinates. This position information is used to reconstruct particle tracks in the detector.⁷

An applied \vec{B} field causes tracks to curve in a helix, giving us information about each particle's momenta. In the transverse plane, this motion is a circle, so from Newton's second law:

⁶LUX-ZEPLIN, a WIMP dark matter direct detection experiment, is essentially one giant TPC. The author of this thesis worked on an ML algorithm for event identification in this TPC.

⁷Ordinary tracking, or 3D tracking, consists of points with 3 spatial coordinates. LHCb has suggested 4D tracking, where each point in a track also has an associated time [14].

$$qvB = m \frac{v_T^2}{R} \quad (1.21)$$

$$qB = \frac{mv_T}{R} \quad (1.22)$$

$$qBR = mv_T = p_T \quad (1.23)$$

where q is the charge of the particle, v_T is the transverse velocity, B is the magnetic field strength, and R is the radius of curvature. The final state particles that reach the TPC will have charge $\pm e$, meaning we can measure the momentum of a charged particle that makes a track in the TPC. The direction the track curves in gives the sign of the charge.

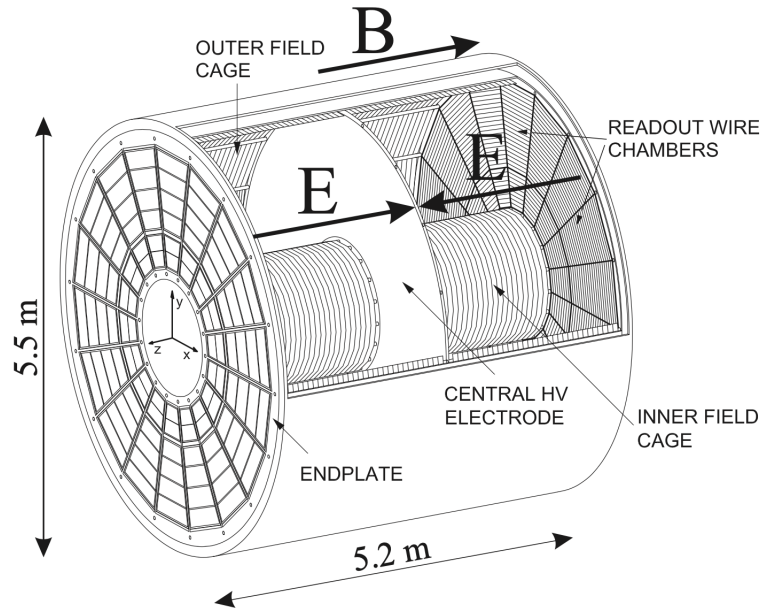


Figure 1.20: A schematic of the ALICE TPC, modified in [15] and originally found in [16]. Note that the TPC is large enough to stand in!

Relativistic charged particles traveling through the TPC lose energy as they interact with the electrons of the gas molecules, inducing ionization of the gas [2]. The mean rate of energy loss for a particle that travels through the medium is given by the Bethe-Bloch equation [17]:

$$\left\langle -\frac{dE}{dx} \right\rangle = K z^2 \frac{Z}{A} \frac{1}{\beta^2} \left[\frac{1}{2} \ln \frac{2m_e c^2 \beta^2 \gamma^2 W_{\max}}{I^2} - \beta^2 - \frac{\delta(\beta\gamma)}{2} \right] \quad (1.24)$$

where $K \approx 0.307 \text{ MeV cm}^2 \text{ mol}^{-1}$ is a constant, z is the charge of the particle in electron charges, Z is the atomic number of the medium, A is the atomic mass of the medium, β is the speed of the particle over c , m_e is the mass of an electron, c is the speed of light, γ is the Lorentz factor, W_{\max} is the maximum kinetic energy the particle can transfer to an electron in the medium in a given collision, I is the mean excitation energy, and δ is a correction term. This gives the energy loss per distance travelled in the medium in terms of properties of the particle and its velocity. This energy loss is measured from the drift electrons collected at the end-plates.

In practice, ALICE utilizes a different parametrization of the Bethe-Bloch formula [18]:

$$f(\beta\gamma) = \frac{P_1}{\beta^{P_4}} \left(P_2 - \beta^{P_4} - \ln \left(P_3 + \frac{1}{(\beta\gamma)^{P_5}} \right) \right) \quad (1.25)$$

where P_{1-5} are parameters determined by the gas mixture in the TPC. Since we can gather information about the particle's momentum from the TPC, this parametrization is commonly written in terms of the mass and momentum of the particle using:

$$\beta = \frac{\gamma m \beta}{\gamma m} = \frac{p}{E} = \frac{p}{\sqrt{m^2 + p^2}} \quad (1.26)$$

where we assume natural units. Thus, if we plot dE/dx against p , each particle will produce a different curve that depends on its mass (Fig. 1.21). With these curves, we can perform particle identification with the TPC. Note that for large p , the curves begin to approach each other, making identification more challenging in this region. In Eq. 1.20, we introduced the idea of a separation power. For the TPC, we calculate a similar—but different—quantity using

$$n_{\sigma, \text{TPC}} = \frac{dE/dx_{\text{meas}} - dE/dx_{\text{exp}}}{\sigma_{\text{TPC}}} \quad (1.27)$$

where dE/dx_{meas} is the measured rate of energy loss, dE/dx_{exp} is the expected rate of energy loss for a given species (calculated from the fits shown in Fig. 1.21), and σ_{TPC} is the resolution of the TPC.

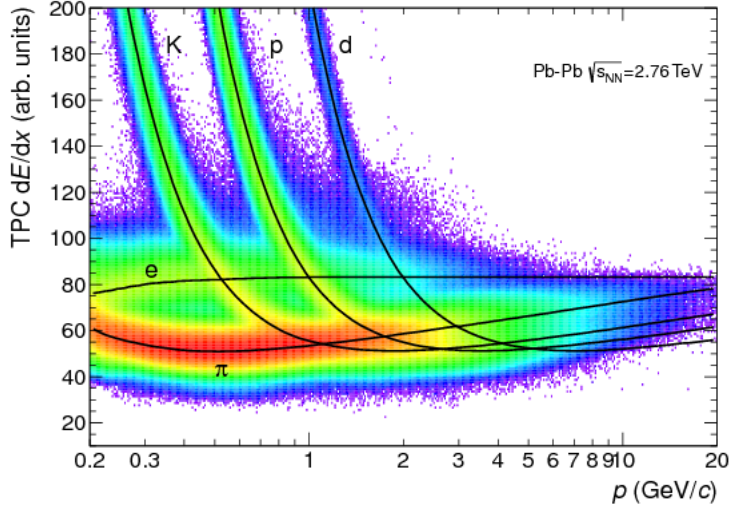


Figure 1.21: The rate of energy loss versus momentum in the TPC. The black lines corresponds to fits using Eq. 1.25

1.4.3 Time-of-Flight (TOF)

The time-of-flight detector (TOF) is used for particle identification and triggers both cosmic ray events and ultraperipheral collisions [19]. The TOF is located 3.7 m, just outside of the TPC, and covers $|\eta| < 0.9$. By measuring the time between the initial interaction and when the particle reaches the TOF, we can reconstruct the particle's velocity. The start time for the TOF to begin the measurement is triggered by the T0 detector [13]. If we let d be the distance from the interaction point to the TOF and Δt be the time between the interaction and when the particle reaches the TOF, then the velocity v of the particle is given by:

$$v = \frac{d}{\Delta t} = \frac{p}{\sqrt{m^2 + p^2}} \quad (1.28)$$

where we use natural units. From Eq. 1.26, we can relate the velocity to the momentum of a particle. Since each particle has a distinct mass, each particle creates a unique band in a plot of v versus p (Fig. 1.22). Additionally, as with the TPC, we can define:

$$n_{\sigma, \text{TOF}} = \frac{\beta_{\text{meas}} - \beta_{\text{exp}}}{\sigma_{\text{TOF}}} \quad (1.29)$$

where β_{meas} is the measured velocity over c in the TOF, β_{exp} is the expected velocity over c , and σ_{TOF} is the resolution of the TOF.

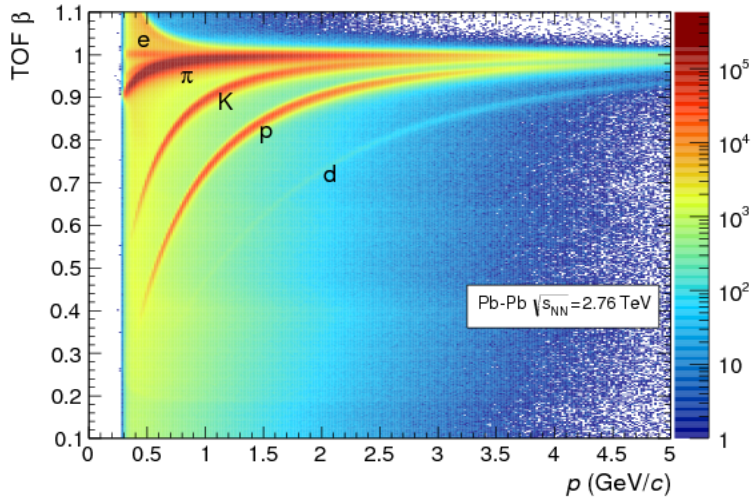


Figure 1.22: β versus p curves from the TOF. Unphysical values of β come from when hits are assigned to the wrong track [19].

1.4.4 Calorimetry

While not necessary for our analysis, a discussion of general collider physics would be remiss without a mention of calorimetry. A *calorimeter* is a detector that measures the energy deposition due to a particle. Some experiments like sPHENIX at the Relativistic Heavy-Ion Collider have both electromagnetic and hadronic calorimeters. In the case of

ALICE, the main calorimeter is the Electromagnetic Calorimeter (EMCal), which is used to identify electrons and photons. The EMCal is also used to detect neutrons and π^0 decays. In particular, the EMCal is important for identifying heavy-flavor electrons that result from semileptonic decays (a weak decay in which a lepton, neutrino, and hadron are produced) [13].

High energy electrons moving through a medium produce bremsstrahlung (braking) radiation. If the bremsstrahlung photon has high enough energy, it can pair produce into an electron and positron, which in turn will produce more bremsstrahlung radiation which causes more pair production. This creates an *electromagnetic shower* which continues until enough energy is lost for pair production to cease (Fig. 1.23). An EMCal utilizes materials with large atomic number as scintillators. Electrons produced in an electromagnetic shower induce light via scintillation, which is measured in sensitive photon detectors [2]. A charged track that enters the EMCal and produces an electromagnetic shower signifies an electron, while a photon might deposit energy in the EMCal without producing a shower. The ALICE EMCal can be used to trigger on events with a jet, by recording an event if the transverse energy in part of the EMCal rises above a certain threshold [13]. In general, hadronic calorimetry is significantly harder because a variable, non-negligible fraction of the incoming hadron's energy goes into undetectable channels [15]. Since ALICE specializes in the identification of low-momentum particles, a hadronic calorimeter is unnecessary.

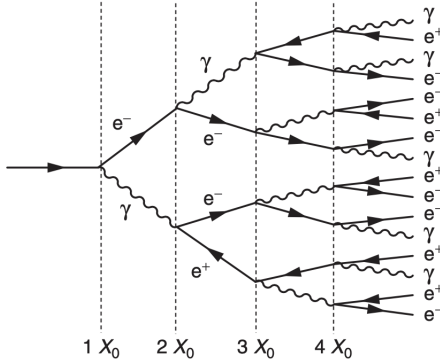


Figure 1.23: A diagram of an electromagnetic shower [2]. Here X_0 represents a characteristic radiation length after which the number of particles doubles.

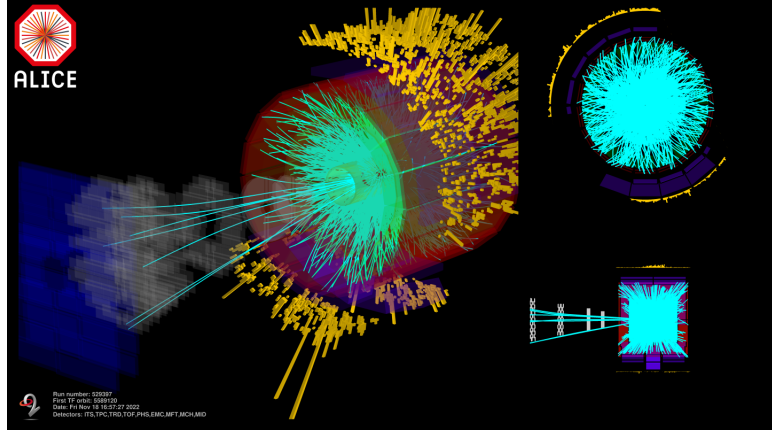


Figure 1.24: Tracks in the ALICE experiment, along with depositions in the calorimeters. This event display is from the start of Run 3 after upgrades to ALICE, including the ITS. The author of this thesis was just starting in heavy-ion physics when these images were released!

1.4.5 VZERO

The VZERO system is composed of the VZERO-A and VZERO-C detectors, which are located in the forward regions at $2.8 < \eta < 5.1$ and $-3.7 < \eta < -1.7$. These detectors are used to trigger events, reject beam-gas interactions, and measure event multiplicity [20]. By measuring energy deposition, the VZERO system can determine the charged particle multiplicity of the event. This is critical in heavy-ion collisions because multiplicity tells us how central or peripheral a collision was.

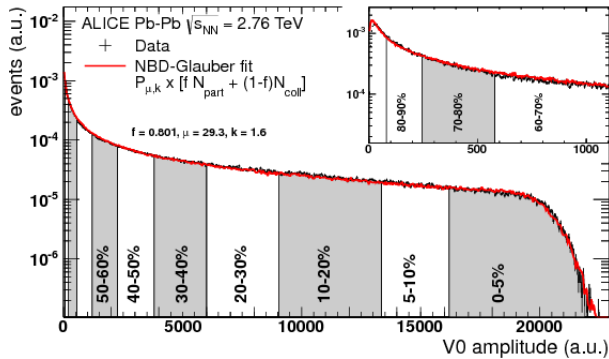


Figure 1.25: The amplitude in the VZERO detector, separated into centrality classes. The Glauber fit refers to the Glauber model, which is used to understand heavy-ion collisions [8].

Chapter 2: Motivations & Methods

Particles on my sweater already.

- Kevin Wen

2.1 Prelude

This thesis is part of a larger effort to elucidate the origins of QGP-like signatures in small systems. To understand this small contribution to the body of knowledge, we first introduce the tools of the trade, then dive into the motivations behind the analysis. This will allow us to fully contextualize our findings which are discussed in the next section.

2.2 A Brief Word on Histogramming

In particle and nuclear physics, histograms form the backbone of much of our analysis. This is because we often seek to determine an underlying probability density from data taken over from a large number of events (ie. collisions). Consider a dataset of N particles, each with some transverse momentum p_T . To construct a 1-D histogram, the horizontal axis, representing p_T is split into intervals called bins or buckets. The y-axis denotes the frequency and is constant within a given bin. For a p_T distribution, the frequency of any given bin is such that the integral over the frequency in that bin yields the total number of particles with p_T lying in the bin. For a p_T distribution, it is common to denote the frequency as dN/dp_T since, for a total number of counts N :

$$N = \int \frac{dN}{dp_T} dp_T \tag{2.1}$$

For a 2-dimensional histogram of p_T and η , we have:

$$N = \int \int \frac{dN}{dp_T d\eta} dp_T d\eta \tag{2.2}$$

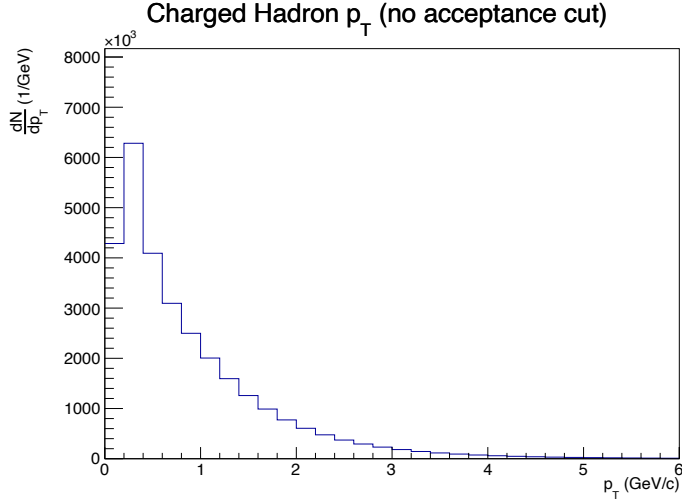


Figure 2.1: A simple p_T distribution of all charged hadrons from our generated data. Notice how the distribution falls off quickly. This means particles that fall within the momentum range of an associated or a trigger particle are relatively rare.

Similary, for arbitrary kinematic variables x_1, \dots, x_N we can construct an N -dimensional histogram where:

$$N = \int \dots \int \frac{dN}{dx_1 \dots dx_N} dx_1 \dots dx_N \quad (2.3)$$

Often, we assume the uncertainty in each bin is \sqrt{n} , where n is the number of counts in a given bin. This comes from the Poisson distribution. While the absolute error in a bin goes as \sqrt{n} , the relative error goes as $\sqrt{n}/n = 1/\sqrt{n}$. Thus, a larger sample gives us better statistics.

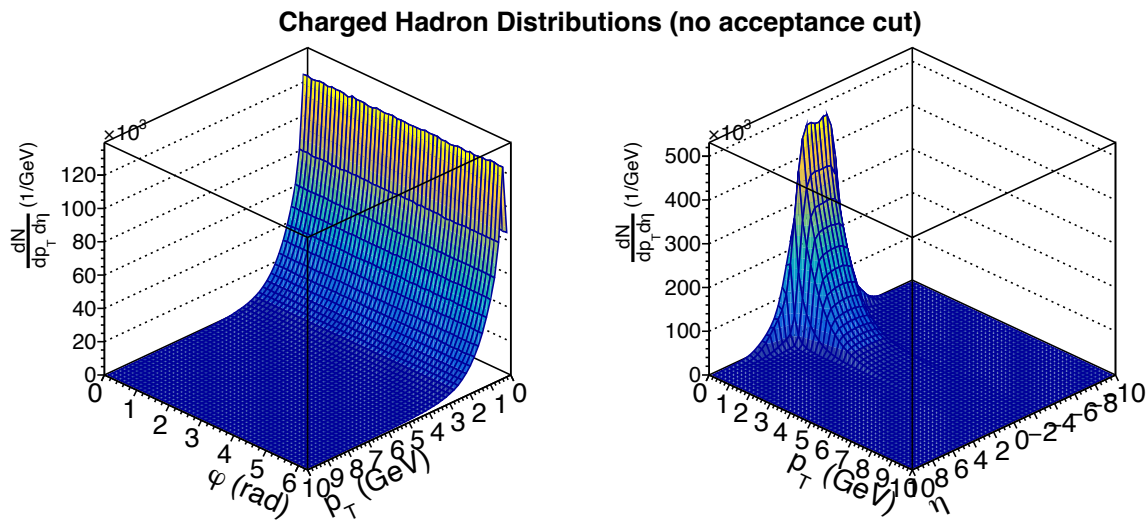


Figure 2.2: Two two-dimensional histograms. The surface and color represent the counts in a given bin. These distributions are not particularly useful, but they demonstrate how particles are distributed in various kinematic variables. In particular, we see particles are evenly distributed in ϕ , and particle production is centered at midrapidity.

2.3 Hadron— Λ Angular Correlations

We are interested in jets because they tell us information about the underlying dynamics between partons. While some physicists fully reconstruct jets to calculate associated observables (eg. two-point energy-energy correlators), we can also gain an understanding of the jet-like structure of events from *two-particle angular correlations*. Rather than performing jet reconstruction, we select for high momentum particles which are assumed to be closely aligned with the jet axis. By correlating these high momentum particles with other particles in the event, we can learn about the structure of jets. To construct an angular correlation, for each event we must:

1. Identify high momentum particles within a certain p_T range: $p_T \in [p_T^{\text{trig, min}}, p_T^{\text{trig, max}}]$. These are referred to as the trigger particles and are assumed to be close to the jet axis since they carry a high p_T .
2. Identify particles within another, typically lower, momentum range $p_T \in [p_T^{\text{assoc, min}}, p_T^{\text{assoc, max}}]$. These are called the associated particles.
3. Take the difference in φ and η for each possible trigger-associated pair. Recall the coordinate system depicted in Fig. 1.6.
4. Fill a $\Delta\varphi\Delta\eta$ distribution with these angle differences.

A basic schematic of these steps is shown in Fig. 2.3. Associated particles comoving with the trigger lead to a peak centered on $\Delta\varphi = 0$, whereas particles moving in the opposite direction of the trigger lead to a peak centered on $\Delta\varphi = \pi$. These peaks are referred to as the *near-side* and *away-side*, respectively. They are the result of dijets, which are the sprays of hadrons produced from the initial hard scattering. The yields and the widths of these peaks thus tell us about the structure of jets in our events. An event might also contain a background of associated particles that are not correlated with the jet, creating a

flat¹ background that the near- and away-side peaks sit on. For example, particles evenly distributed in φ would create this background.

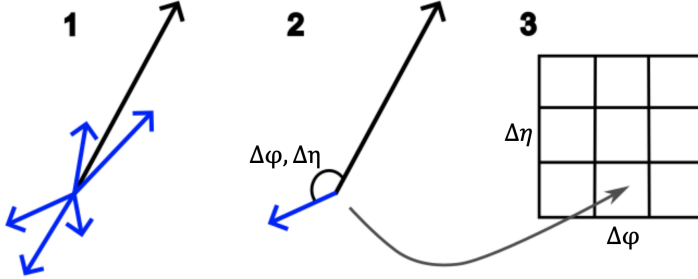


Figure 2.3: A basic diagram representing how a 2D angular correlation is performed. The black arrow represents a trigger particle and the blue arrows represent associates in the dijet. By taking pairwise differences in φ and η between the trigger and associated particles, we construct a 2D distribution. Note that typically there is also an uncorrelated background from associated particles that are not in the jet. These are not drawn here for simplicity.

Broadly, we think of the near- and away-side as representing hard physics from initial interactions involving high four-momentum transfers between partons. The underlying event, which comes from particles not correlated to the jet, originates from two main sources. The first is soft scatterings—additional or secondary scatterings that do not result from the initial hard scattering. For example, a QGP in Pb-Pb would contribute to the underlying event via soft scatterings of partons within the medium. The second source comes from events with multiple hard scatterings or jets. If there are multiple triggers (jets) in the event, then some jet-like signal will contribute to the underlying event.

We select certain particle species to serve as the trigger and associated particles, depending on what physics we are probing. A hadron—hadron correlation utilizes hadrons as the trigger and associated particles while a hadron— Λ correlation utilizes hadrons as the trigger and Λ 's as the associated. Often, we project a 2D $\Delta\varphi\Delta\eta$ distribution into a 1D distribution in $\Delta\varphi$. This is referred to as an azimuthal, angular, or $\Delta\varphi$ correlation. For

¹In some analyses, flow adds a small sinusoid to the flat background. This is not relevant to our analysis here.

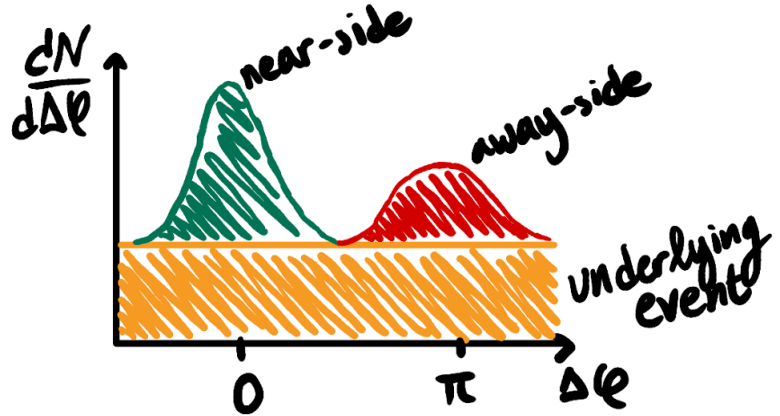


Figure 2.4: A cartoon of an azimuthal correlation. The near-side and away-side represent the jet-like structure of the selected events, and the underlying event gives information about soft physics.

this thesis, we only need the $\Delta\varphi$ distribution; however, structures in $\Delta\eta$ give us important information.

Typically, the away-side of a $\Delta\varphi$ distribution is wider than the near-side. We can think of dijets as the leading order type of jet that we observe; however, there are also three-pronged pronged jets at next leading order (and so on). Since the trigger defines the jet-axis, the away-side gets smeared by these three-pronged jets. In addition, quarks can radiate gluons and gluons can split, knocking partons off the jet axis and broadening the away-side.

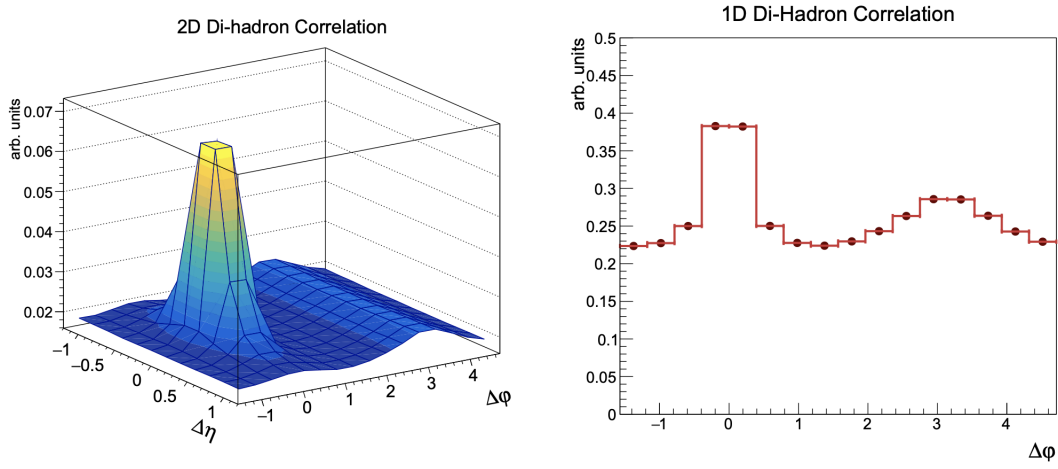


Figure 2.5: An example of a 2D angular correlation and its projection into a 1D $\Delta\phi$ distribution. Taken from [21].

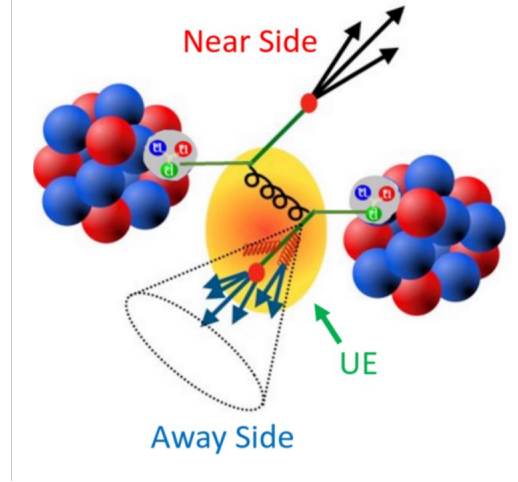


Figure 2.6: A heavy-ion collision featuring a hard scattering between two partons. This produces two jets, one of which experiences the medium. When we select for events high momentum, we suffer from *surface bias*. This is because dijets that begin near the center of the medium will be fully quenched. It's simply more likely we measure an event where the near-side jet experienced a small path length through the medium while the away-side traveled through a larger length of QGP. This fact is depicted in the cartoon.

2.4 PYTHIA

PYTHIA is an event generator used to simulate high energy collisions. An event is the result of a collision, essentially a list of particles with their kinematic information. To simulate an event, PYTHIA combines both calculations from first principles and ones involving measured parameters—making PYTHIA a data-driven model. In total, PYTHIA relies on the order of 100 parameters [22]. Ideally, PYTHIA outputs what an ideal detector would measure, one without a limited acceptance or subject to efficiencies. As a result, PYTHIA is commonly compared with data, allowing high energy physicists to estimate how many particles the detector could not measure and to compare theoretical models with data.

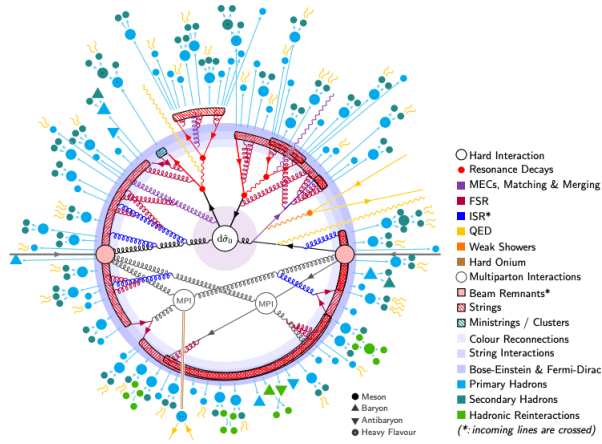


Figure 2.7: The structure of a PYTHIA8 event, decreasing in hardness scale from the initial hard scattering to the final state.

Hadron-hadron collisions are extremely messy, complicated processes, making a full analytic description of such events impossible. Instead, we use numerical methods to generate an event with a certain probability of occurring.² At its heart, PYTHIA relies on Markov Chain Monte Carlo methods which in turn rely on a pseudo-random number generator. In essence, this allows PYTHIA to capture the random nature of events, which are fundamentally subject to quantum mechanical probabilities. There are three "levels" to a given

²It's much harder to get a Higgs out of an event, approximately only 1 in a billion p-p events at the LHC contain a Higgs.

PYTHIA event:

1. Process Level: This describes the initial hard-scattering and resonances.³ Due to the high Q^2 , this level relies on perturbative methods.
2. Parton Level: This describes the evolution of the parton shower and multi-parton interactions. This level yields the partonic structure of jets and the underlying event.
3. Hadron Level: This handles the confinement of partons into hadrons. Hadronization is modeled by QCD strings that fragment into hadrons. These hadrons can then undergo further decays and scatterings. Hadronization cannot rely on perturbative models. This level yields the hadrons an ideal detector would measure.

A diagram of a PYTHIA event is shown in Fig. 2.7, with the stages ordered by hardness scale, but we can think of this as time. The outermost particles, the final-state hadrons, should capture what an ideal detector would measure. PYTHIA is incredibly complex, with multiple layers. Simulating the evolution of partons into color-neutral hadrons is not trivial.

2.5 Motivation

This thesis complements an ALICE PhD dissertation that sought to measure strangeness production in and out of jets in p-Pb events at the LHC. This is motivated by the discovery of collective effects in small systems like p-p and p-Pb which questions our understanding of QGP formation and heavy-ion collisions. High multiplicity p-Pb collisions at the LHC show the same strangeness enhancement as low multiplicity Pb-Pb (Fig. 1.16), prompting us to investigate the origins of strangeness enhancement. By probing the mechanisms behind strangeness production in p-Pb, we can better understand strangeness enhancement, contributing to our understanding of the limits of QGP formation.

³Short-lived particles like the top quark. These must be produced early in the collision, so they are associated with the initial hard-scattering.

As part of this ALICE study, h- Λ correlations were constructed from ALICE p-Pb data. Taking the Λ hyperon as the associated allows for calculating the yields of strange particles inside of jets (the near- and away-side peaks) and outside of jets (underlying event). The strangeness production in the underlying event represents soft processes⁴, which allows us to probe possible QGP formation by separating strangeness enhancement into three distinct regions. In addition, the widths of the near- and away-side were calculated from fits. Since strangeness enhancement is evaluated relative to non-strange hadron production, h-h correlations were also constructed. The ratios of widths and yields—strange over non-strange—were evaluated as a function of multiplicity. This enabled an evaluation of strangeness enhancement. This type of analysis was first performed on the $\phi(1020)$ meson, an $s\bar{s}$ pair [21]. The $\phi(1020)$ has closed strangeness ($|S| = 0$), while the Λ^0 has $|S| = 1$, which makes comparisons between the measurements of both species interesting.

Due to the finite acceptance of ALICE, this analysis required a cut of $|\eta| < 0.8$. This is smaller than the acceptance of the TPC to avoid edge effects. If strangeness production outside of this acceptance is different from production inside, this would alter our correlations, requiring us to perform corrections. Since hadron collisions are complicated, we do not know *a priori* if this effect is negligible. We have to perform a systematic check with a model like PYTHIA.

2.6 Analysis Description

In this thesis, we analyze the effect of detector acceptance on h- Λ angular correlations. To accomplish this, we first generated 10 million PYTHIA6 p-p events at $\sqrt{s} = 7$ TeV. These events are biased to have virtually no underlying event, meaning that all final-state hadrons result from the hard scattering. This allows for clear separation of the near- and away-side. Out of *all* particles produced in our events, we obtained approximately 15% π^\pm , 11% π^0 , 4% K^\pm , 4% K^0 , 0.3% protons, and 2% electrons.

⁴Assuming nearly all selected events have one trigger, which was verified.

We then construct $h-\Lambda$ and $h-h$ distributions for three acceptances, represented by a pseudorapidity cut on the associate: $|\eta_{\text{assoc}}| < 0.8, 1.2, 2.0$. This corresponds to slowly widening the acceptance of the ALICE experiment. The acceptance cut on the trigger is fixed to $|\eta_{\text{trig}}| < 0.8$. We fix the cut on the trigger because the trigger selects for the relevant physics, and we are interested in the midrapidity region where particle production from the hard scattering is concentrated. Note that an η cut leads to a cut in $\Delta\eta$, but a $\Delta\eta$ cut is not necessarily a cut on η . We take $4 < p_T^{\text{trig}} < 8 \text{ GeV}/c$ and $2 < p_T^{\text{assoc}} < 4 \text{ GeV}/c$. From Fig. 2.1, we see particles within these p_T ranges are relatively rare. By hadron, we refer to charged hadrons, specifically protons, K^\pm , π^\pm , electrons, and their corresponding antiparticles. This is simply because ALICE primarily measures charged particles. By Λ , we mean the Λ^0 and its antiparticle. The selection of particle species is consistent with the previously mentioned analysis. For each acceptance, we calculate the ratio of the near- and away-side widths and yields between the $h-\Lambda$ and $h-h$ distributions. We take the ratio because we are interested in the relative production of Λ hyperons to hadrons. Recalling the Wroblewski ratio, since the final-state charged hadrons are mostly π^\pm this is comparable to other measurements of strangeness enhancement.

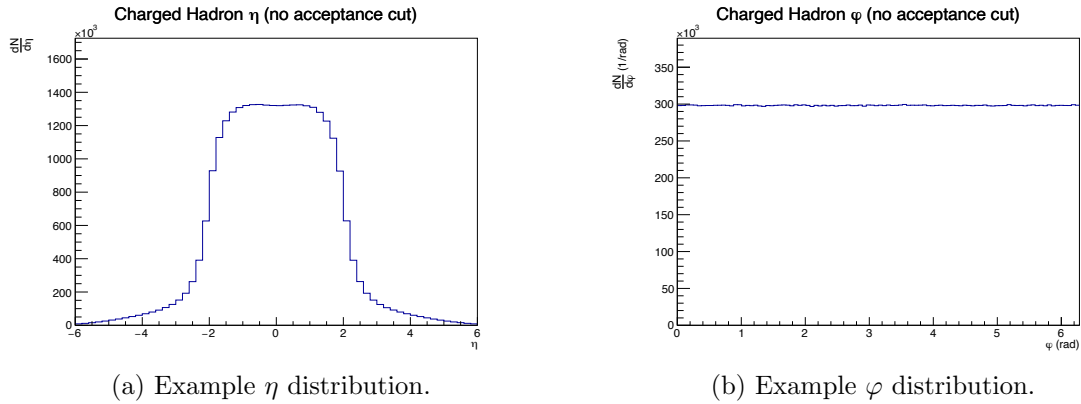


Figure 2.8: Example distributions of η and φ , constructed with charged hadrons from our generated events. A cut on η would chop the η distribution. In addition, notice how φ is flat, meaning particles are uniformly distributed in the transverse plane.

Since the selected events have nearly no background, the near- and away-side peaks

are clearly separated. Thus, for calculating yields, the near-side is taken as all counts within $\Delta\varphi \in [-\frac{\pi}{2}, \frac{\pi}{2}]$ and the away-side is defined as $\Delta\varphi \in [\frac{\pi}{2}, \frac{3\pi}{2}]$. Thus, the yields are defined as:

$$Y_{\text{NS}} = \int_{-\frac{\pi}{2}}^{\frac{\pi}{2}} \frac{dN}{d\Delta\varphi} d\Delta\varphi \quad (2.4)$$

$$Y_{\text{AS}} = \int_{\frac{\pi}{2}}^{\frac{3\pi}{2}} \frac{dN}{d\Delta\varphi} d\Delta\varphi \quad (2.5)$$

where Y_{NS} is the yield in the near-side peak and Y_{AS} is the yield in the away-side peak. If the peaks were not so well separated, we would need to define more stringent ranges. Fits are performed with a double Gaussian, and the procedure is outlined below. For each acceptance, we then calculate the ratios:

$$\frac{Y_{\text{NS}}^{\text{h}-\Lambda}}{Y_{\text{NS}}^{\text{h-h}}} \text{ and } \frac{Y_{\text{AS}}^{\text{h}-\Lambda}}{Y_{\text{AS}}^{\text{h-h}}} \quad (2.6)$$

where the superscript represents the type correlation we calculate the yield for. As with the standard measurement of strangeness enhancement, we divide the h— Λ distribution by the h—h distribution. Similarly, we assign widths to the near- and away-side peaks via fits. These widths are calculated from the standard deviation of the fit, giving us the ratios:

$$\frac{\sigma_{\text{NS}}^{\text{h}-\Lambda}}{\sigma_{\text{NS}}^{\text{h-h}}} \text{ and } \frac{\sigma_{\text{AS}}^{\text{h}-\Lambda}}{\sigma_{\text{AS}}^{\text{h-h}}} \quad (2.7)$$

This fit procedure requires care, so we use the next section to elaborate in detail.

2.7 Fitting Procedure

While yields can be calculated by simply integrating over each distribution, the widths must be calculated from a fit. To fit each $\Delta\varphi$ distribution, we used the default ROOT fit method which minimizes χ^2 :

$$\chi^2 = \sum_i \left(\frac{y(i) - f(x_i)}{\sigma(i)} \right)^2 \quad (2.8)$$

where i is the bin number, $y(i)$ is the value of the data at bin i , $x(i)$ is the bin center, f is the fit function, and $\sigma(i)$ is the error in bin i . To characterize the goodness-of-fit, we introduce the idea of the number of degrees of freedom (NDF) for a fit:

$$\text{NDF} = n - k \quad (2.9)$$

where n is the number of data points and k is the number of free fit parameters. As a rule of thumb, a good fit is one where $\chi^2/\text{NDF} \approx 1$. We display χ^2/NDF on all fits.

To ascribe a width to our distributions, we chose a double Gaussian as our fit function:

$$\frac{dN}{d\Delta\varphi} = A_{\text{NS}} \exp \left(\frac{-1}{2} \left(\frac{\Delta\varphi - \mu_{\text{NS}}}{\sigma_{\text{NS}}} \right)^2 \right) \quad (2.10)$$

$$+ A_{\text{AS}} \exp \left(\frac{-1}{2} \left(\frac{\Delta\varphi - \mu_{\text{AS}}}{\sigma_{\text{AS}}} \right)^2 \right) \quad (2.11)$$

where A is the amplitude of each Gaussian, μ is the mean of each Gaussian, and σ is the standard deviation of each Gaussian. Since each Gaussian is fitting a peak that originates from the jet-like structure of the events, we fix $\mu_{\text{NS}} = 0$ and $\mu_{\text{AS}} = \pi$. This physics consideration reduces the degrees of freedom in the fit by 2. In Fig. 2.12, we show an example of this fit. The standard deviation of a Gaussian gives us the measure of its width. While a Gaussian fit function is a natural choice, it is not the only one. To ensure the fits are stable and accurately capture the width of the distribution, we also used the generalized Gaussian and Von Mises fit functions. The generalized Gaussian is given by:

$$f(x) = \frac{\beta}{2\alpha\Gamma(1/\beta)} \exp \left(- \left(\frac{|x - \mu|}{\alpha} \right)^\beta \right) \quad (2.12)$$

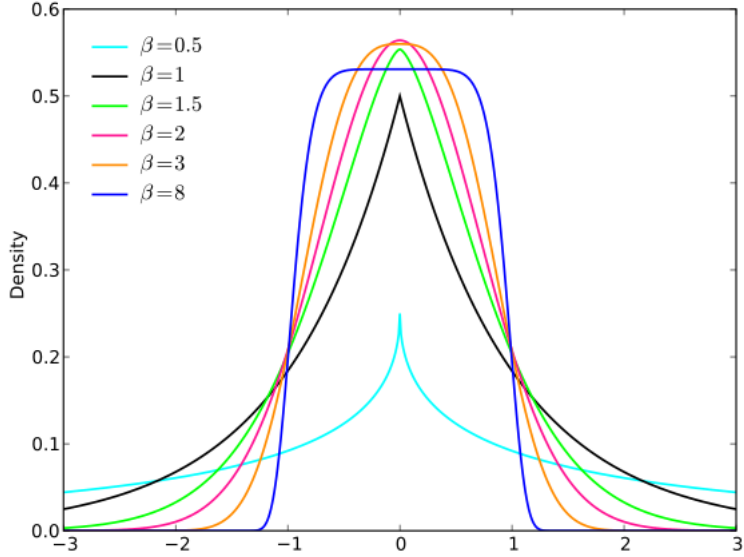


Figure 2.9: A depiction of the generalized gaussian probability density for various values of β . We see that *beta* controls how sharply peaked the distribution is. From: *Wikipedia*.

where β is the shape parameter, α is the scale parameter, μ gives the location of the mean, and Γ is the gamma function. Notice that for $\beta = 2$, the generalized Gaussian is the Gaussian distribution. Again, we fit a sum of generalized Gaussians to each $\Delta\varphi$ distribution. As with the double Gaussian, one mean is fixed to 0 and the other to π . The standard deviation for the generalized Gaussian is:

$$\sigma = \sqrt{\frac{\alpha^2 \Gamma(3/\beta)}{\Gamma(1/\beta)}} \quad (2.13)$$

Fundamentally, a $\Delta\varphi$ correlation is a distribution wrapped on a circle, which is the focus of *directional statistics*.⁵ This is because φ is an angle on a circle, so $\Delta\varphi$ is also periodic. Figures like Fig. 2.4 are slightly deceptive because they do not explicitly show the distribution is wrapped on the circle. There is no difference between $\Delta\varphi = -\frac{\pi}{2}$ and

⁵Statistics on the circle is tricky. Naively, the average of 364° and 1° is 182.5° , but we know it should be 0° .

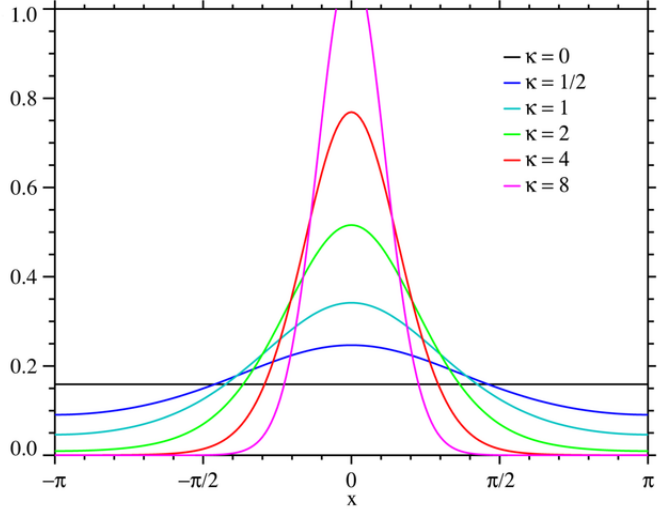


Figure 2.10: The Von Mises distribution for various values of κ , the concentration parameter. Source: *Wikipedia*.

$\Delta\varphi = \frac{3\pi}{2}$. The Von Mises is a natural choice because it is a periodic approximation to the Gaussian distribution. The Von Mises probability density function is given by

$$f(x) = \frac{\exp(\kappa \cos(x - \mu))}{2\pi I_0(\kappa)} \quad (2.14)$$

where κ is the concentration parameter, μ is the location, and I_0 is the modified Bessel function of the first kind of order zero. Since $\cos(x)$ and $I_0(x)$ are 2π -periodic, the Von Mises distribution is intrinsically periodic, unlike the Gaussian and generalized Gaussian. This makes the Von Mises an appealing choice. From Fig. 2.10, we see that $1/\kappa$ is like the standard deviation and μ is an angle that behaves like the mean. Furthermore, a small value of κ corresponds to a uniform distribution (not concentrated), while a large value of κ creates a sharply peaked distribution (concentrated). Again, we fix $\mu = 0$ for the near-side and $\mu = \pi$ for the away-side. In order to compare widths with the Gaussian and generalized Gaussian fits, we need to translate κ into a circular standard deviation. Since we are in the territory of directional statistics, this requires great care.

Consider a finite distribution of points on the unit circle, much like our $\Delta\varphi$ distributions. To characterize the spread of these points, we can associate the position of each point

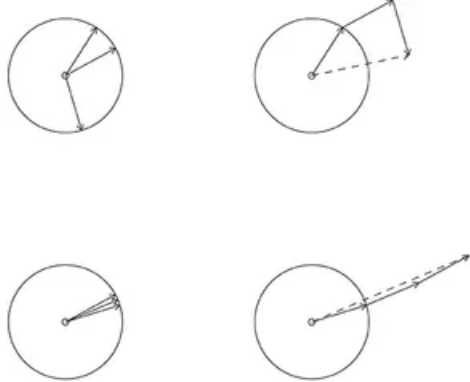


Figure 2.11: The left column represents two circular, or directed, datasets. A unit vector points to data points on the circle. By taking the resultant of these unit vectors, we can estimate the spread of the data. Image from [23].

with a vector, and take the sum of these vectors, as shown in Fig. 2.11. If our points on the circle are highly concentrated, the resultant vector will attain a large magnitude; however, if our points are highly spread, the resultant vector will have a magnitude nearly zero. To quantify this, we define the mean resultant length:

$$R = \frac{1}{N} \left\| \sum_i \vec{R}_i \right\| \quad (2.15)$$

where \vec{R}_i are the unit vectors representing each data point, and N is the total number of points. This is simply the magnitude of the resultant vector divided by the number of points. One can show that $R \in [0, 1]$, where a value of $R = 0$ indicates highly spread data, while a value of $R = 1$ corresponds to a highly concentrated dataset. This allows us to define the mean circular variance:

$$V = 1 - R \quad (2.16)$$

so $V = 0$ means concentrated data and $V = 1$ represents a spread dataset. This is closer to a typical variance we would associate to a dataset on \mathbb{R} . It is important to note

that⁶

$$\sigma \neq \sqrt{V} \quad (2.17)$$

We can extend these ideas to a continuous distribution. For a wrapped normal distribution, a Gaussian in a variable $x \pmod{2\pi}$, we find

$$R = \exp \frac{-1}{2}\sigma^2 \quad (2.18)$$

where σ is the circular standard deviation associated with the wrapped normal distribution. Thus,

$$\sigma = \sqrt{\ln(-2R)} \quad (2.19)$$

The wrapped normal distribution closely approximates the Von Mises distribution, meaning we can use this definition to associate a linear standard deviation to the Von Mises. For the Von Mises distribution,

$$R = \frac{I_1(\kappa)}{I_0(\kappa)} := A_1(\kappa) \quad (2.20)$$

Finally, for the Von Mises, this implies the correct standard deviation is

$$\sigma = \sqrt{\ln(-2A_1(\kappa))} \quad (2.21)$$

This is the standard deviation we compute to compare with the Gaussian and generalized Gaussian fits. For all fits, the near- and away-side are simultaneously fitted and the means are fixed. In summary, the standard deviations we use to compare widths between fits are:

⁶However, for $\sigma \ll 1$, $\sigma \approx \sqrt{2V}$. This is obtained from a simple Taylor expansion.

Fit Function	Standard Deviation
Gaussian	σ
Generalized Gaussian	$\sqrt{\frac{\alpha^2 \Gamma(3/\beta)}{\Gamma(1/\beta)}}$
Von Mises	$\sqrt{\ln(-2A_1(\kappa))}$

For each acceptance, we calculate the ratios:

$$\frac{\sigma_{\text{NS}}^{\text{h-L}}}{\sigma_{\text{NS}}^{\text{h-h}}} \text{ and } \frac{\sigma_{\text{AS}}^{\text{h-L}}}{\sigma_{\text{AS}}^{\text{h-h}}} \quad (2.22)$$

The final results for these ratios are calculated from the double Gaussian fits. In the next section, we also compare these results with the double generalized Gaussian and double Von Mises fits. An example of these fit functions is displayed in Fig. 2.12, which demonstrates the different shapes of each function. For details concerning error propagation and all fits, see Appendix A.

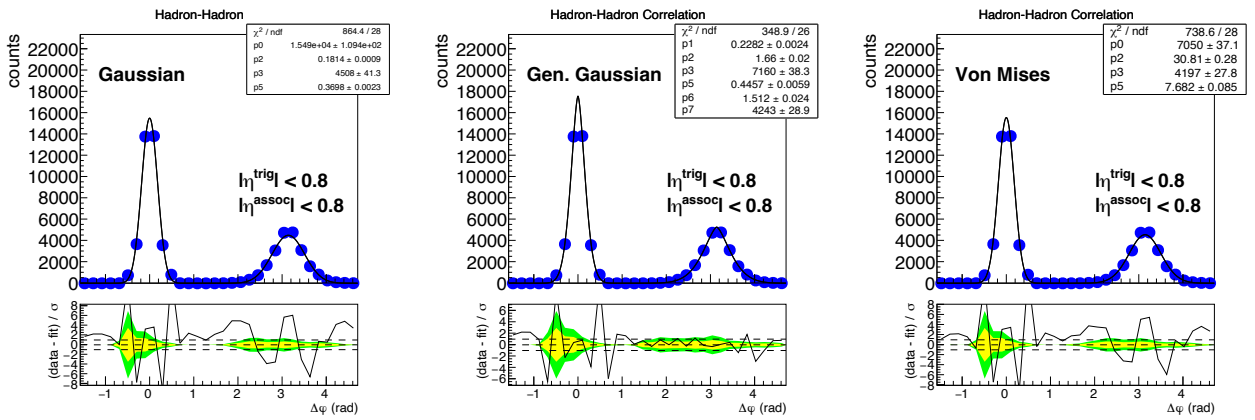


Figure 2.12: Examples of various fits on a $h-h$ distribution with an acceptance cut of $|\eta| < 0.8$. The graphs under each distribution represent terms in the χ^2 formula, indicating where the fit describes the data well. The yellow band represents one σ and the green band shows two σ . For this particular correlation, we see the generalized Gaussian describes the away-side quite well. The Gaussian and Von Mises cannot adequately capture the peak of the away-side. Since $\beta \neq 2$, this could indicate the near- and away-side are not truly Gaussian.

Chapter 3: Results & Discussion

Nuclear spaghetti.

- *Unknown*

3.1 Generated Distributions

An example of both a h—h and h— Λ correlation, generated from our PYTHIA6 events, are shown in Fig. 3.1 and Fig. 3.2, respectively. We also include projections of relevant kinematic variables to demonstrate the cuts used to construct an angular correlation. All fits are shown in Appendix A.

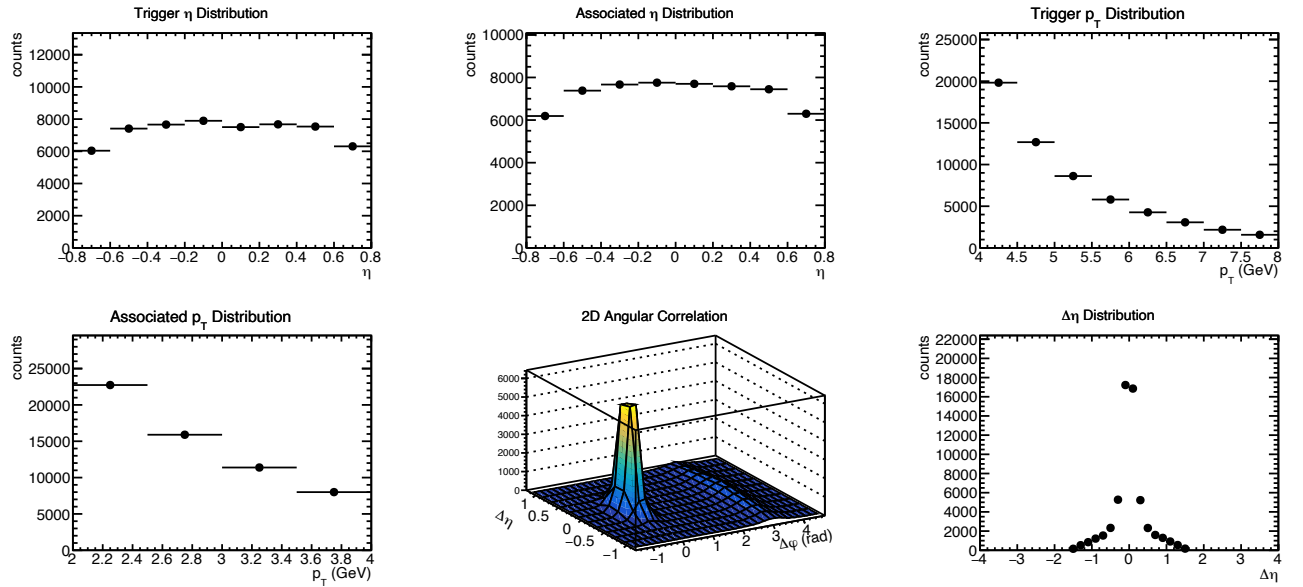


Figure 3.1: A h—h correlation for $2 < p_T^{\text{assoc}} < 4$, $4 < p_T^{\text{assoc}} < 8$, and $|\eta| < 0.8$. All single-particle distributions are constructed from particles that are counted in the 2D angular correlation. We see the η distributions are abruptly cut off at $\eta = \pm 0.8$, and the p_T distributions also display cuts. The $\Delta\eta$ distribution is a projection of the 2D angular correlation.

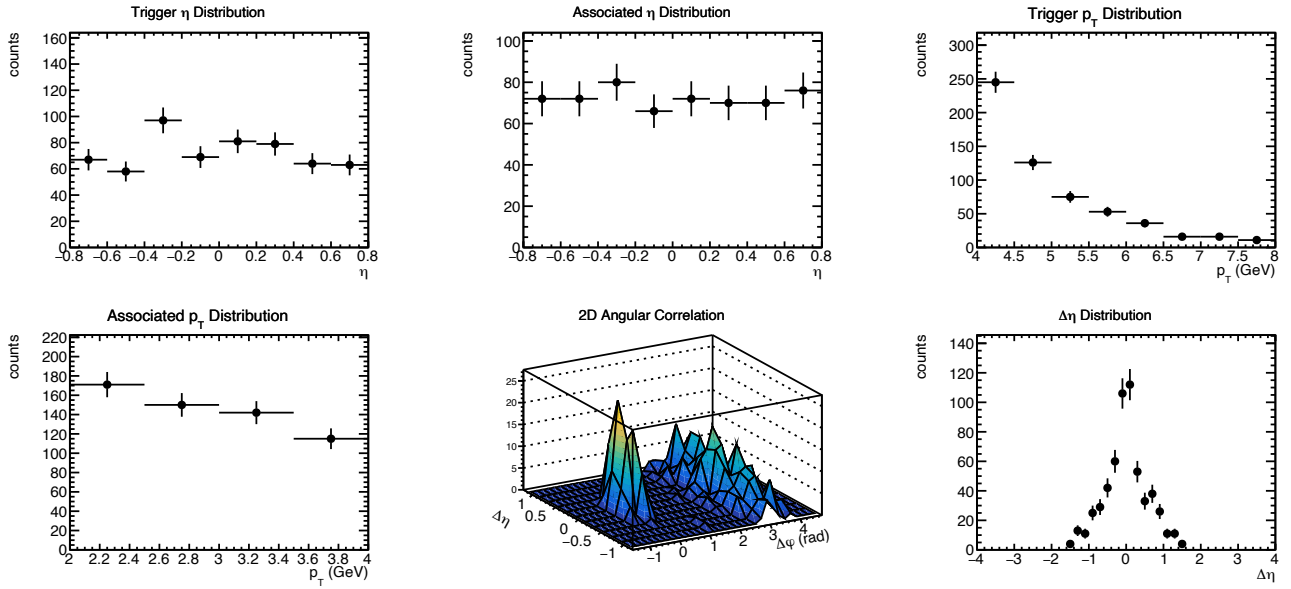


Figure 3.2: A $h-\Lambda$ correlation for $2 < p_T^{\text{assoc}} < 4$, $4 < p_T^{\text{assoc}} < 8$, and $|\eta| < 0.8$. Note we have much more statistics for the $h-h$ distribution.

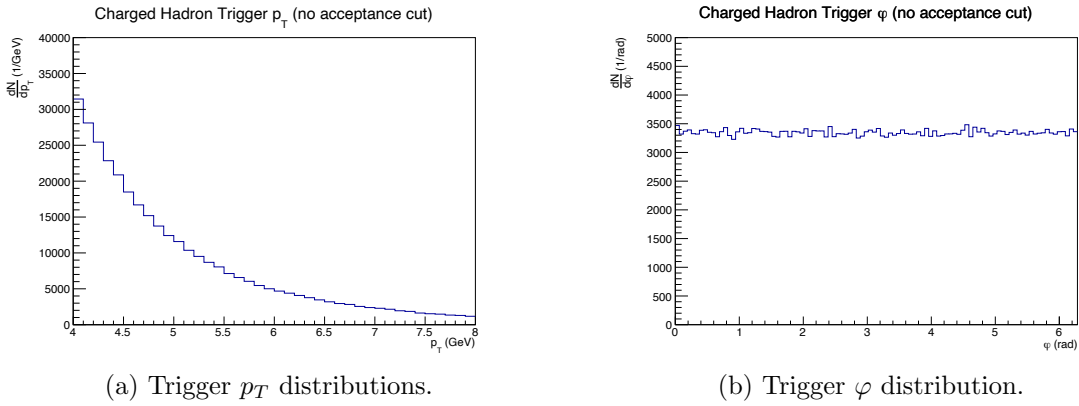


Figure 3.3: The p_T and φ distributions for all trigger hadrons. From Fig. 2.1, we see that very few charged hadrons are within the trigger p_T range.

3.2 Yields

The yield ratios for the near- and away-side are shown for each acceptance. These yields are a simple sum of the counts in each bin within a peak, so the uncertainty is simply the principal root of the yield. For all ratios, errors are propagated via the standard propagation of uncertainty, assuming no correlation between variables. From Fig. 3.4, we see the yield ratios agree across all acceptances. Thus, no systematic corrections are needed for the yield ratios. We also calculated the yield ratios for more acceptance cuts, which we include in Appendix B.

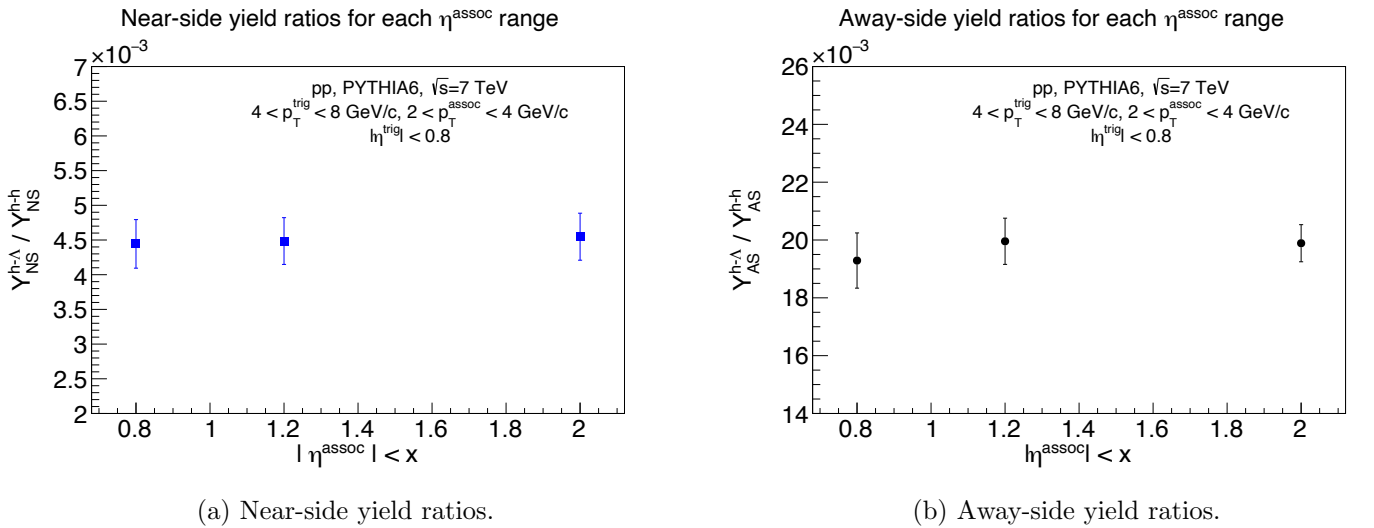


Figure 3.4: Yield ratios for each η cut on the associated. Both the yield ratios on the near- and away-side agree across all cuts.

3.3 Widths

The width ratios for each acceptance are presented across all acceptances in Fig. 3.5. The width here is simply the standard deviation from the double Gaussian fit. We see the width ratios agree for all acceptances, indicating no further systematic corrections are required. For each distribution, we also calculate the ratio of the away-side to near-side width (Fig. 3.6). The near-side is chosen as the normalization since the trigger serves as the jet-axis proxy. In addition, the away-side is quenched in heavy-ion collisions, so normalizing by the near-side lets us compare. We find a slight downward trend for both the $h-\Lambda$ and $h-h$ correlations as the acceptance is opened, although more statistics are needed to make a robust physics interpretation. The downward trend suggests the away-side broadens more slowly than the near-side. Since a tight cut on η modifies the p_T spectrum by introducing a bias towards midrapidity, this trend could result from a p_T dependence.

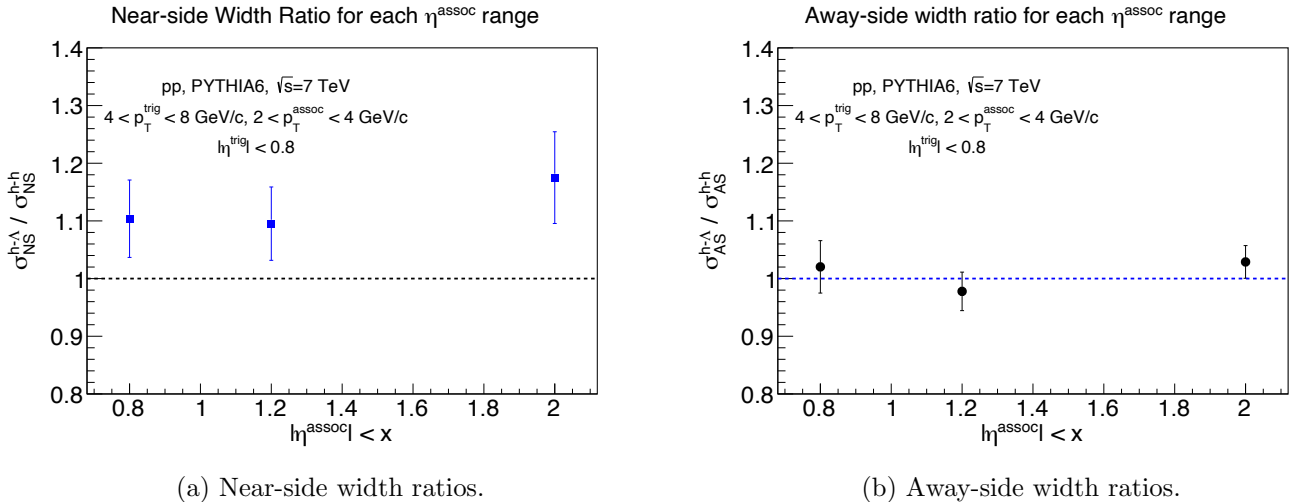


Figure 3.5: Width ratios for each η cut on the associated. Both the width ratios on the near- and away-side agree across all cuts.

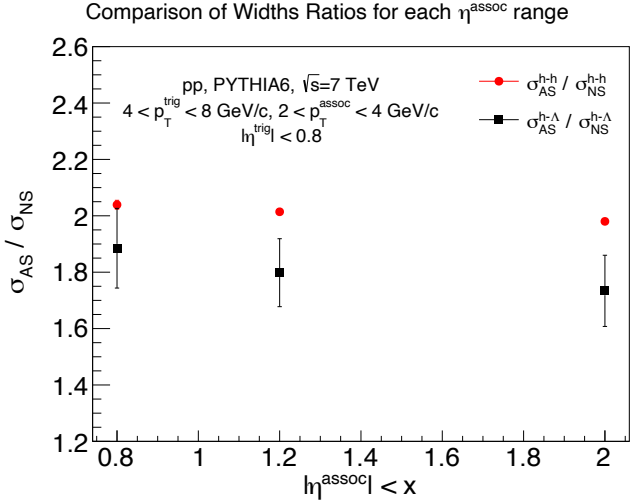


Figure 3.6: Near-side widths over away-side widths for each η cut and distribution.

3.4 Evaluation of Fit Stability

All experiments and analyses involve choices; even if they are good choices, they can impact results in subtle ways. Systematic errors attempt to quantify these uncertainties that do not arise from statistical fluctuations. Since the choice of fit function is somewhat arbitrary, we must ensure the extracted widths truly reflect the spread of each peak. The Gaussian function seems like a good choice since it is quite common and seems simpler than the generalized Gaussian and Von Mises, but there is no obvious reason to choose the Gaussian. As a systematic check, we also calculate widths and width ratios using the generalized Gaussian and Von Mises. If these widths and ratios are in general agreement, we can be confident in the values we assign to the widths—this is a systematic check. All fits are included in Appendix A, and an example of the various fit functions is shown in Fig. 2.12.

We show the fitted widths from each fit function across acceptances in Fig. 3.7 and the corresponding width ratios in Fig. 3.8. The results are quite close between all fits, indicating that our fits are stable. In Fig. 3.7, the value of σ agrees for all fits on the near-side, and $\text{h}-\Lambda$ away-side. For the away-side of the $\text{h}-\text{h}$ distribution, the generalized Gaussian predicts consistently higher widths than the Von Mises and Gaussian distributions. A close

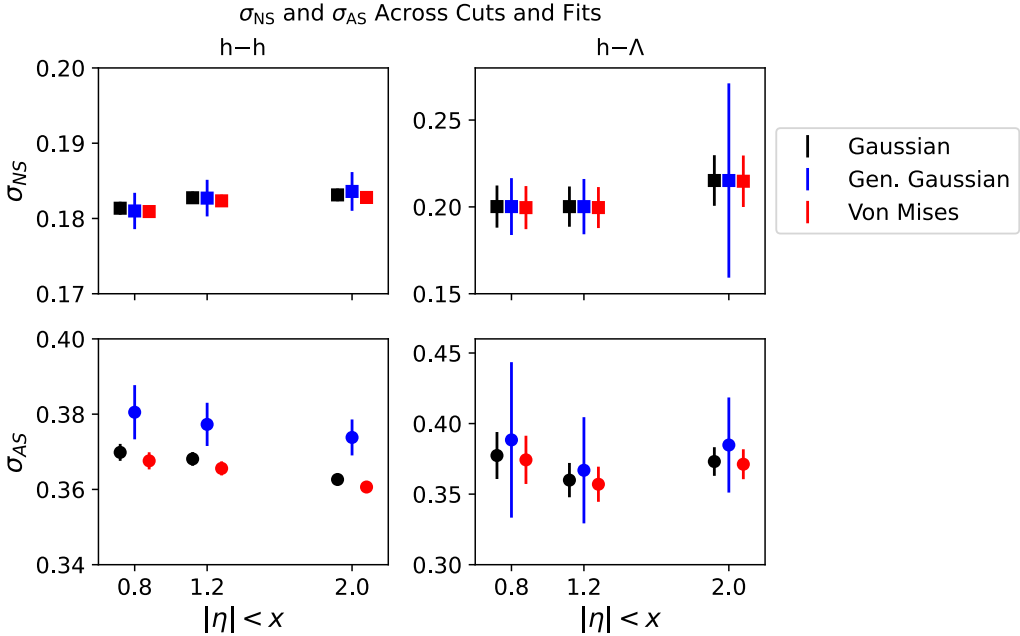


Figure 3.7: Near- and away-side widths for each fit function and distribution. We see the widths are in general agreement. Note the vertical axes do not start at zero.

inspection of the fits reveals the $h-h$ away-side is slightly triangular, which the generalized Gaussian can capture with its flexibility in shape. The errors on the widths calculated from the generalized Gaussian are consistently larger than those from the Gaussian and Von Mises fits. This is likely an overestimate of the error and requires closer inspection. This could result from a correlation between α and β , meaning we would need to account for more elements of the covariance matrix when propagating errors. We suspect this is an overestimate because the calculated width ratios are extremely close. Any disagreement in the measure of the absolute widths cancels in the ratios. Thus, we use the Gaussian distribution for our final results because it is the "simplest" distribution. In reality, this choice is arbitrary but does not affect the interpretation that our acceptance cut does not artificially modify our correlations.

In many fits shown in Appendix A, the χ^2/NDF values are lower for the $h-\Lambda$ distributions. At face value, this indicates a better fit; however, we must consider that there are many more high p_T hadrons than Λ hyperons. Consequently, the relative uncertainty in

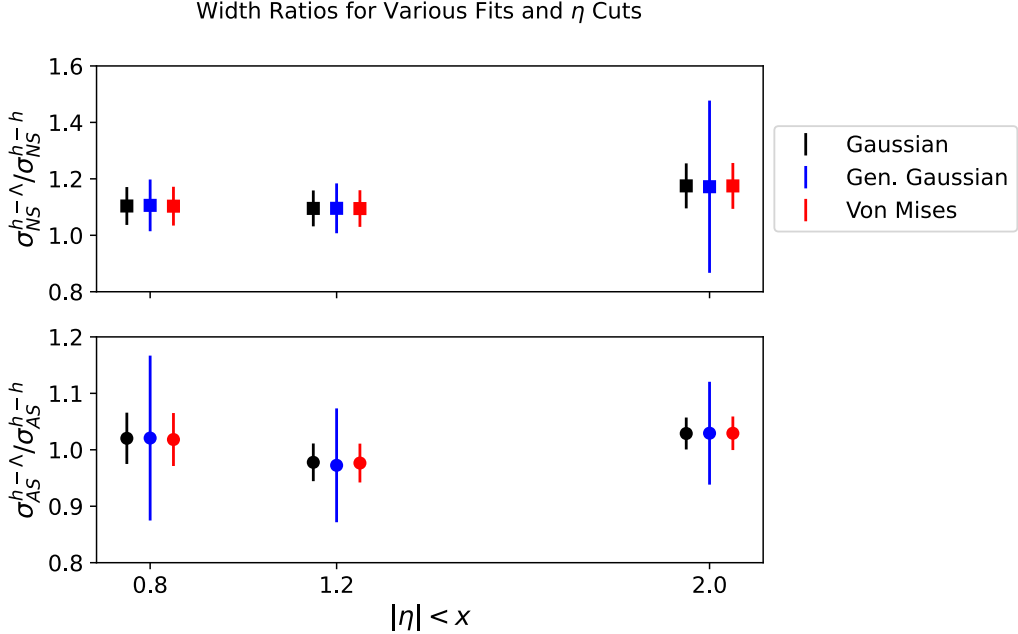


Figure 3.8: Near- and away-side width ratios for each fit function and distribution. The horizontal axis represents each of the three η cuts. We see the fits mostly agree and any disagreement cancels in the width ratios.

each bin of our $h-h$ distributions is much lower than for the $h-\Lambda$ correlation. Due to larger uncertainties, a fit can describe the $h-\Lambda$ distribution much more easily, and the χ^2 value is driven down. On the other hand, a fit must describe the $h-h$ distributions exceptionally well for the χ^2 to not blow up due to minuscule uncertainties. We expect the fits of the $h-\Lambda$ correlations would worsen with more statistics. From a physics standpoint, fragmentation need not produce Gaussian correlations, and our $h-h$ distributions are certainly not entirely Gaussian. We only use fit functions that are Gaussian-like, so we should expect similar extracted widths. In other words, the fact that our width ratios are similar across fit functions does not necessarily indicate goodness-of-fit. This is a potential weakness that could be addressed with a different choice of fit function. However, since the fits are stable and generally capture the width of near- and away-side, we can still interpret the widths of our correlations. We find that the width ratios are not affected by acceptance, given the choice of fit.

3.5 Future Work

We would like to further investigate strangeness production by comparing simulations of p-Pb to data. While p-p events offer a good baseline to isolate acceptance-dependent effects, we can still learn much more about strangeness enhancement in p-Pb. In particular, we are interested in the event generator Parton-Hadron-String Dynamics (PHSD), which aims to capture the microscopic aspects of events [24]. In PHSD, we aim to study how strangeness production differs for various types of strange hadrons.

Chapter 4: Summary

In high energy heavy-ion collisions, the temperatures and densities necessary to create the quark-gluon plasma (QGP) are reached. This is a state of matter where the partons ordinarily bound inside color-neutral hadrons are deconfined. The QGP is thought to have filled the universe microseconds after the Big Bang and provides a probe of quantum chromodynamics (QCD) at extreme energy densities. While physicists expected QGP formation in relativistic heavy-ion collisions, we did not expect a medium in small systems. However, measured collective effects in these small systems indicate possible droplets of QGP. To study the limits of QGP formation, we focus on strangeness enhancement, the relative increase in production of strange quarks (compared to up and down quarks) as system size increases. This is an important signature of QGP production. High multiplicity p-Pb events reach the level of strangeness enhancement seen in low-multiplicity Pb-Pb, demanding an investigation of strangeness production in p-Pb. An analysis on behalf of the ALICE collaboration used $h-\Lambda$ angular correlations to separate production of strange quarks in and out of jets. Due to the finite acceptance of ALICE, this required a pseudorapidity cut of $|\eta| < 0.8$. In this thesis, we evaluate the effect of acceptance on the widths and yields of $h-\Lambda$ and $h-h$ correlations. Using p-p PYTHIA6 events at $\sqrt{s} = 7$ TeV, we find no significant effects from the limited acceptance of ALICE. The yields agree for all η cuts. Similarly, the widths are evaluated using multiple fit functions, which show broad agreement. The ratios of these widths and yields, calculated as $h-\Lambda$ over $h-h$ (strange over non-strange), are consistent across all fits and acceptances.

Chapter 5: Resources for the Aspiring Undergraduate Researcher

This is a list of useful resources for undergraduates beginning their journey in heavy-ion physics.

- **CERN ROOT Software.** This is the software you will utilize for the actual analysis. There are many tutorials available. Learn to read the documentation, and it will help you later! URL: <https://root.cern/>
- **Nevis Labs ROOT Tutorial.** Great, comprehensive tutorial to learn ROOT. Covers both some aspects of ROOT in C++ and Python. <https://www.nevis.columbia.edu/~seligman/root-class/>
- **Physics Matters ROOT Tutorials.** A great playlist to learn ROOT from install to histogram arithmetic. URL: <https://www.youtube.com/watch?v=KPz-dNjdx40&list=PLLybgCU6QCGWLdD04ZDaB0kLr03maeYAe>
- **CERN Courier.** Subscribe to the magazine. URL: <https://cerncourier.com/>
- **InspireHEP.** A place for high energy physicists to share articles, list conferences, and more. This is really just a good place to check what people are publishing and find articles. URL: <https://inspirehep.net/>
- **arXiv.** A magical place in physics where pre-prints are uploaded. This is the spirit of open-access. URL: <https://arxiv.org/>
- **Ultrarelativistic Heavy-Ion Collisions by Ramona Vogt.** A great introductory book to heavy-ion collisions. The material is hard, but certain sections are enriching.
- **Phenomenology of Ultra-Relativistic Heavy-Ion Collisions by Wojciech Florkowski.** A more advanced book on heavy-ion collisions. The first chapter is a great introduction with links to experiment.

- **Modern Particle Physics by Mark Thomson.** A superb introduction to modern particle physics with basic explanations of colliders, Feynman diagrams, and theory. If you've taken Quantum II, this is a great resource.
- **Detectors in Particle Physics: A Modern Introduction by Viehhauser and Weidberg.** If you're tired of number crunching, read this book. It covers experimental methods in particle physics in great detail and with broad scope. URL: <https://inspirehep.net/literature/2767057>
- **Particle Data Group.** For basic figures, PDG codes, and measured parameters. URL: <https://pdg.lbl.gov/>
- **Spacetime Physics by Taylor and Wheeler.** A good introduction to special relativity. I haven't read this book, but I've heard good things. URL: <https://www.eftaylor.com/spacetimephysics/>
- **A Beginners Course in General Relativity by Bernard Schutz.** The first chapter has a good, brief coverage of special relativity if you are already somewhat familiar with the subject.
- **Quantum Mechanics: A Paradigms Approach by David McIntyre.** This is a superb book for quantum mechanics. Most of my intuition for quantum phenomena from the idea of an abstract state to perturbation theory comes from this book. The exercises are great too. I cannot recommend it enough.
- **Heavy-Ion Collisions: The Big Picture, and the Big Questions.** For a big-picture overview of the field. This review is dense for someone just starting, but it would be beneficial to take a peek at some point. URL: <https://arxiv.org/abs/1802.04801>.

Appendix A: Fits

A.1 Double Gaussian

Explicitly, the double Gaussian fit is given by:

$$\frac{dN}{d\Delta\varphi} = A_{\text{NS}} \exp\left(\frac{-1}{2} \left(\frac{\Delta\varphi - \mu_{\text{NS}}}{\sigma_{\text{NS}}}\right)^2\right) \quad (\text{A.1})$$

$$+ A_{\text{AS}} \exp\left(\frac{-1}{2} \left(\frac{\Delta\varphi - \mu_{\text{AS}}}{\sigma_{\text{AS}}}\right)^2\right) \quad (\text{A.2})$$

where σ is the standard deviation, μ is the mean, and the subscripts on the fitted parameters indicate the near- and away-side. The uncertainty in σ is simply obtained from the fit. All double Gaussian fits are shown in Fig. A.1.

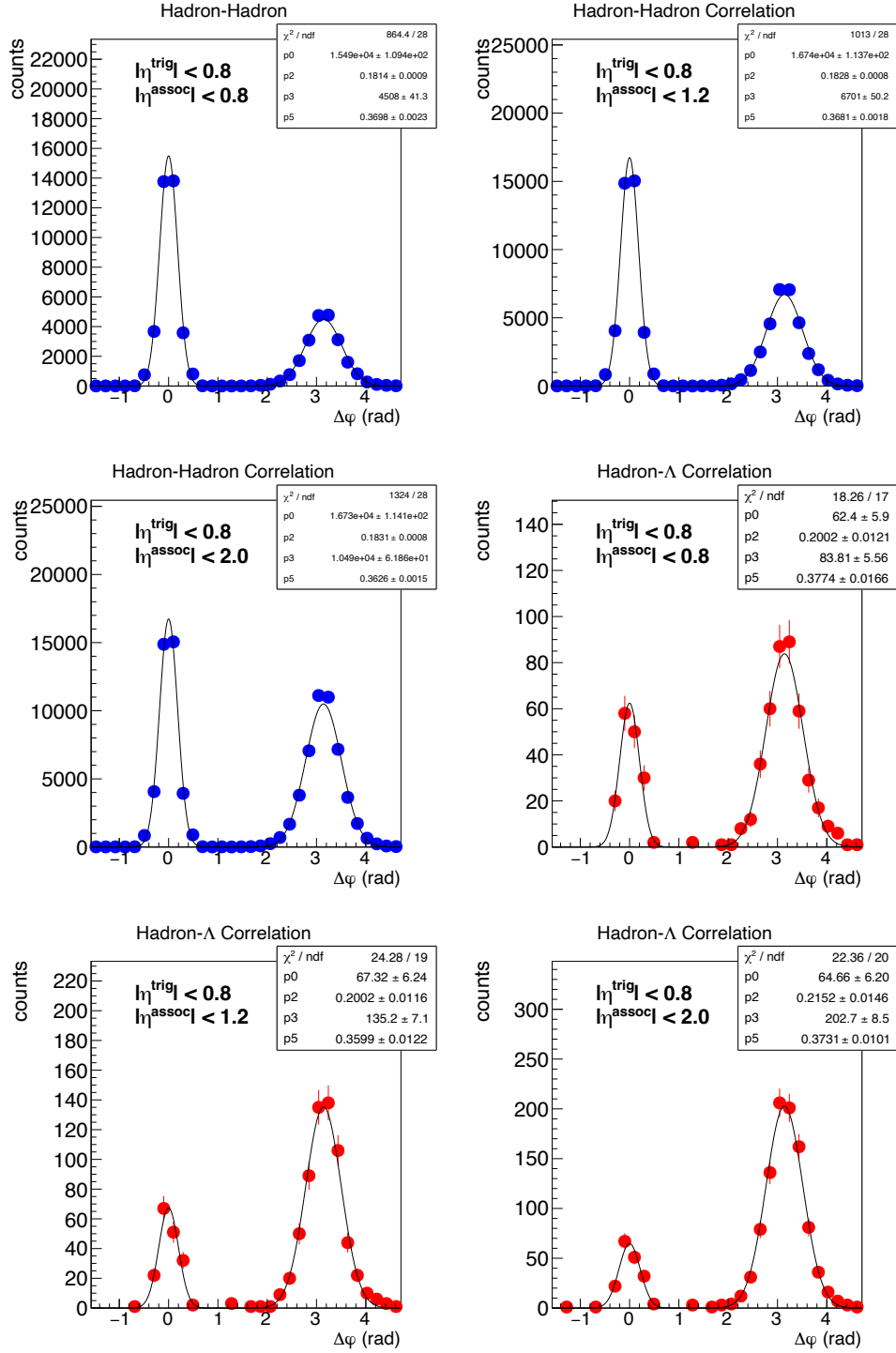


Figure A.1: Gaussian fits for all correlations. In order, the fit parameters are A_{NS} , σ_{NS} , A_{AS} , and σ_{AS} .

A.2 Double Generalized Gaussian

$$\frac{dN}{d\Delta\varphi} = A_{\text{NS}} \frac{\beta_{\text{NS}}}{2\alpha_{\text{NS}}\Gamma(1/\beta_{\text{NS}})} \exp\left(-\left(\frac{|x - \mu_{\text{NS}}|}{\alpha_{\text{NS}}}\right)^{\beta_{\text{NS}}}\right) \quad (\text{A.3})$$

$$+ A_{\text{AS}} \frac{\beta_{\text{AS}}}{2\alpha_{\text{AS}}\Gamma(1/\beta_{\text{AS}})} \exp\left(-\left(\frac{|x - \mu_{\text{AS}}|}{\alpha_{\text{AS}}}\right)^{\beta_{\text{AS}}}\right) \quad (\text{A.4})$$

where α , β , and μ are fit parameters explained in Section 2.7, and the subscripts denote whether the term fits the near- or away-side. The standard deviation from this fit is given in Eq. 2.13. For a given generalized Gaussian, the uncertainty in the standard deviation is given by

$$s_\sigma = \sqrt{\left(\frac{\partial\sigma}{\partial\alpha}\sigma_\alpha\right)^2 + \left(\frac{\partial\sigma}{\partial\beta}\sigma_\beta\right)^2} \quad (\text{A.5})$$

where s_σ is the uncertainty in the standard deviation, σ is the standard deviation, and σ_α and σ_β are the uncertainties in the fit parameters. All double generalized Gaussian fits are shown in Fig. A.2. To explicitly write these partial derivatives, we must introduce the polygamma function of order zero, also known as the digamma function:

$$\psi(x) = \frac{\Gamma'(x)}{\Gamma(x)} \quad (\text{A.6})$$

so that

$$\frac{\partial\sigma}{\partial\alpha} = \frac{\sigma}{\alpha} \quad (\text{A.7})$$

$$\frac{\partial\sigma}{\partial\beta} = \frac{\sigma}{2\beta^2}(\psi(1/\beta) - 3\psi(3/\beta)) \quad (\text{A.8})$$

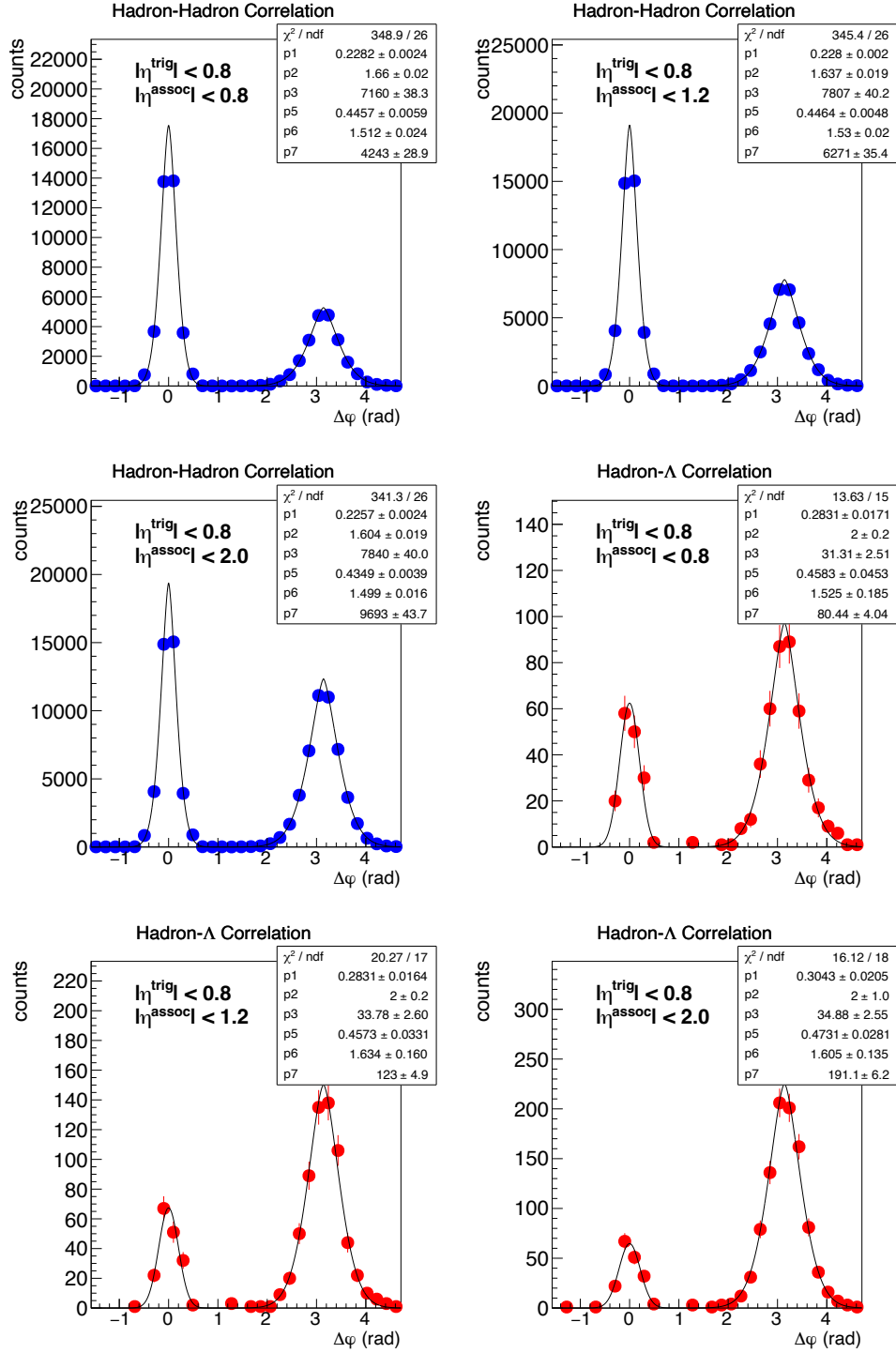


Figure A.2: Generalized Gaussian fits for all correlations. In order, the fit parameters are α_{NS} , β_{NS} , A_{NS} , α_{AS} , β_{AS} , A_{AS} .

A.3 Double Von Mises

$$\frac{dN}{d\Delta\varphi} = A_{\text{NS}} \frac{\exp(\kappa_{\text{NS}} \cos(x - \mu_{\text{NS}}))}{2\pi I_0(\kappa_{\text{NS}})} \quad (\text{A.9})$$

$$+ A_{\text{AS}} \frac{\exp(\kappa_{\text{AS}} \cos(x - \mu_{\text{AS}}))}{2\pi I_0(\kappa_{\text{AS}})} \quad (\text{A.10})$$

where κ and μ are fit parameters explained in Section 2.7. These fits are shown in Fig. A.3. For the Von Mises, the uncertainty in the standard deviation is simply:

$$s_\sigma = \frac{\partial\sigma}{\partial\kappa}\sigma_\kappa = \frac{1}{\sigma} \left(\frac{I_1}{I_0} - \frac{I_0}{I_1} + \frac{1}{\kappa} \right) \sigma_\kappa \quad (\text{A.11})$$

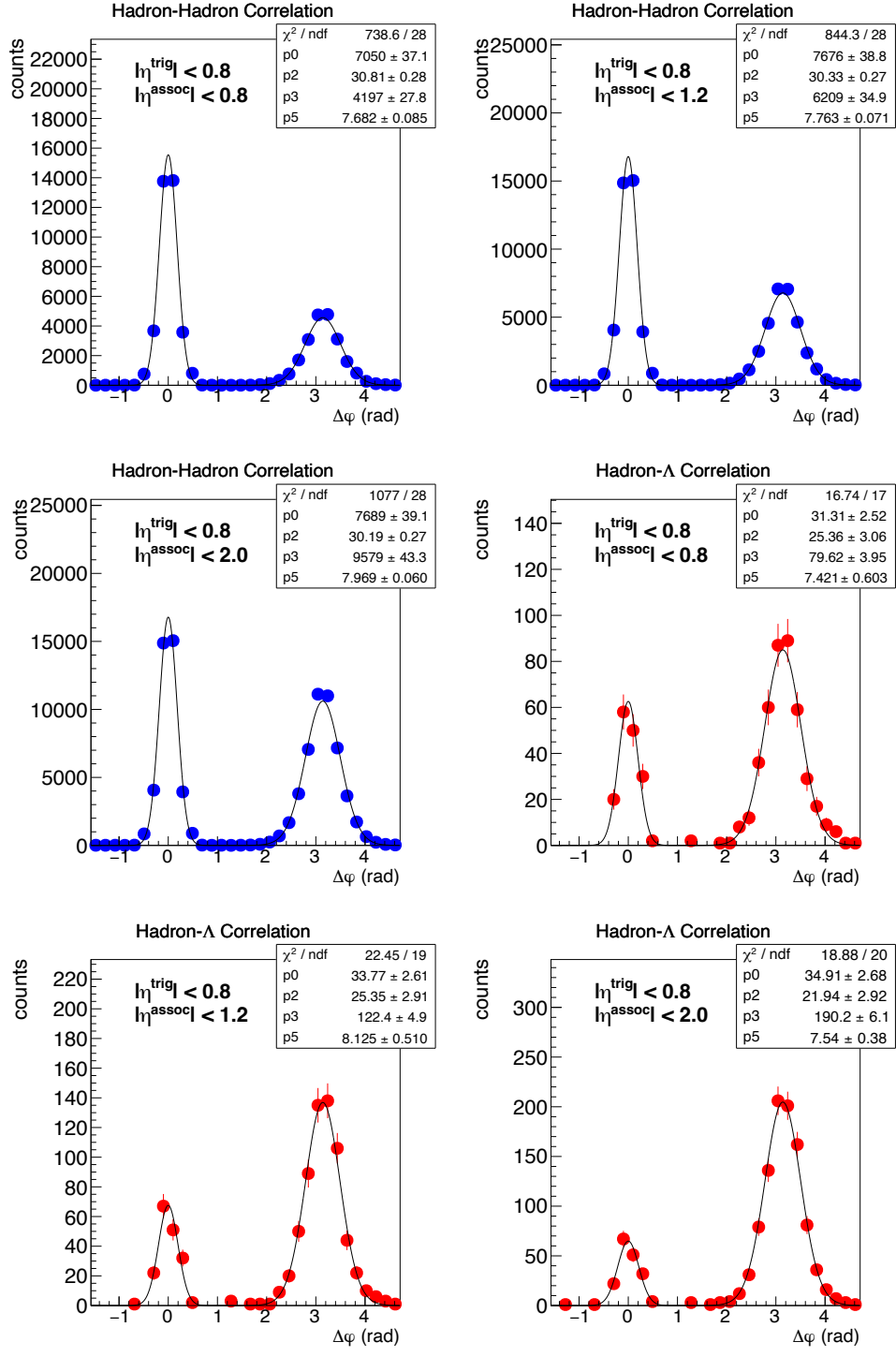


Figure A.3: Von Mises fits for all correlations. In order, the fit parameters are A_{NS} , κ_{NS} , and A_{AS} .

Appendix B: Dense Yield Ratios

For thoroughness, we also include yield ratios for more η cuts. These are then fitted to a simple linear fit, and we find the slopes agree with 0, indicating no measurable effects from acceptance.

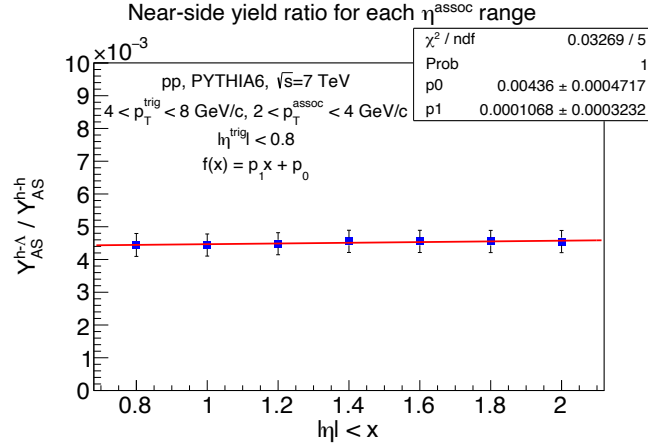


Figure B.1: Yield ratios for the near-side across many η cuts on the associated. The slope agrees with zero.

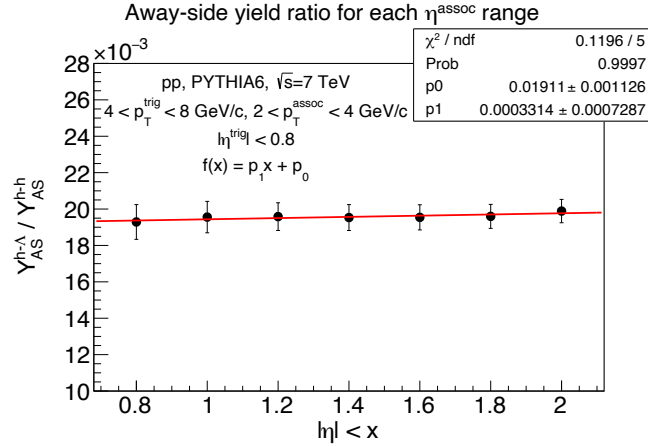


Figure B.2: Yield ratios for the away-side across many η cuts on the associated. The slope agrees with zero.

Works Cited

- [1] R. L. Workman et al. “Review of Particle Physics”. In: *PTEP* 2022 (2022), p. 083C01. DOI: [10.1093/ptep/ptac097](https://doi.org/10.1093/ptep/ptac097).
- [2] Mark Thomson. *Modern particle physics*. New York: Cambridge University Press, 2013. ISBN: 978-1-107-03426-6. DOI: [10.1017/CBO9781139525367](https://doi.org/10.1017/CBO9781139525367).
- [3] Ramona Vogt. *Ultrarelativistic heavy-ion collisions*. Amsterdam: Elsevier, 2007. ISBN: 978-0-444-52196-5.
- [4] Wit Busza, Krishna Rajagopal, and Wilke van der Schee. “Heavy Ion Collisions: The Big Picture, and the Big Questions”. In: *Ann. Rev. Nucl. Part. Sci.* 68 (2018), pp. 339–376. DOI: [10.1146/annurev-nucl-101917-020852](https://doi.org/10.1146/annurev-nucl-101917-020852). arXiv: [1802.04801 \[hep-ph\]](https://arxiv.org/abs/1802.04801).
- [5] Ani Aprahamian et al. “Reaching for the horizon: The 2015 long range plan for nuclear science”. In: (Oct. 2015).
- [6] Michael Strickland. “Anisotropic Hydrodynamics: Three lectures”. In: *Acta Phys. Polon. B* 45.12 (2014). Ed. by Michal Praszalowicz, pp. 2355–2394. DOI: [10.5506/APhysPolB.45.2355](https://doi.org/10.5506/APhysPolB.45.2355). arXiv: [1410.5786 \[nucl-th\]](https://arxiv.org/abs/1410.5786).
- [7] Alberica Toia. “Participants and spectators at the heavy-ion fireball”. 2013. URL: <https://cerncourier.com/a/participants-and-spectators-at-the-heavy-ion-fireball/#:~:text=To%20see%20how%20much%20of,to%20the%20most%20central%20collisions..>
- [8] Wojciech Florkowski. *Phenomenology of Ultra-Relativistic Heavy-Ion Collisions*. Mar. 2010. ISBN: 978-981-4280-66-2.
- [9] P. Achenbach et al. “The Present and Future of QCD”. In: (Mar. 2023). arXiv: [2303.02579 \[hep-ph\]](https://arxiv.org/abs/2303.02579).
- [10] Johann Rafelski and Berndt Muller. “Strangeness Production in the Quark - Gluon Plasma”. In: *Phys. Rev. Lett.* 48 (1982). [Erratum: *Phys.Rev.Lett.* 56, 2334 (1986)], p. 1066. DOI: [10.1103/PhysRevLett.48.1066](https://doi.org/10.1103/PhysRevLett.48.1066).

- [11] K. Aamodt et al. “The ALICE experiment at the CERN LHC”. In: *JINST* 3 (2008), S08002. doi: [10.1088/1748-0221/3/08/S08002](https://doi.org/10.1088/1748-0221/3/08/S08002).
- [12] Arturo Tauro. “ALICE Schematics”. General Photo. 2017. URL: <https://cds.cern.ch/record/2263642>.
- [13] Betty Bezverkhny Abelev et al. “Performance of the ALICE Experiment at the CERN LHC”. In: *Int. J. Mod. Phys. A* 29 (2014), p. 1430044. doi: [10.1142/S0217751X14300440](https://doi.org/10.1142/S0217751X14300440). arXiv: [1402.4476 \[nucl-ex\]](https://arxiv.org/abs/1402.4476).
- [14] “Framework TDR for the LHCb Upgrade II: Opportunities in flavour physics, and beyond, in the HL-LHC era”. In: (2021).
- [15] Georg Viehhauser and Tony Weidberg. *Detectors in Particle Physics : A Modern Introduction*. Taylor & Francis, 2024. ISBN: 978-1-00-386157-7, 978-1-00-386163-8, 978-1-03-224658-1, 978-1-00-328767-4. doi: [10.1201/9781003287674](https://doi.org/10.1201/9781003287674).
- [16] J. Alme et al. “The ALICE TPC, a large 3-dimensional tracking device with fast read-out for ultra-high multiplicity events”. In: *Nucl. Instrum. Meth. A* 622 (2010), pp. 316–367. doi: [10.1016/j.nima.2010.04.042](https://doi.org/10.1016/j.nima.2010.04.042). arXiv: [1001.1950 \[physics.ins-det\]](https://arxiv.org/abs/1001.1950).
- [17] H. Bichsel, Donald E. Groom, and S. R. Klein. “Passage of particles through matter”. In: (July 2004).
- [18] Weilin Yu. “Particle identification of the ALICE TPC via dE/dx”. In: *Nucl. Instrum. Meth. A* 706 (2013). Ed. by P. Fusco et al., pp. 55–58. doi: [10.1016/j.nima.2012.05.022](https://doi.org/10.1016/j.nima.2012.05.022).
- [19] Francesca Carnesecchi. “Performance of the ALICE Time-Of-Flight detector at the LHC”. In: *JINST* 14.06 (2019), p. C06023. doi: [10.1088/1748-0221/14/06/C06023](https://doi.org/10.1088/1748-0221/14/06/C06023). arXiv: [1806.03825 \[physics.ins-det\]](https://arxiv.org/abs/1806.03825).
- [20] E. Abbas et al. “Performance of the ALICE VZERO system”. In: *JINST* 8 (2013), P10016. doi: [10.1088/1748-0221/8/10/P10016](https://doi.org/10.1088/1748-0221/8/10/P10016). arXiv: [1306.3130 \[nucl-ex\]](https://arxiv.org/abs/1306.3130).
- [21] Justin Blair. “Investigating the origin of strangeness enhancement using jet-like [eta] – [phi] angular correlations in p-Pb Collisions with ALICE”. Other thesis. 2023-04-19, Texas U., U. Texas, Austin (main), Apr. 2023.

- [22] Christian Bierlich et al. “A comprehensive guide to the physics and usage of PYTHIA 8.3”. In: *SciPost Phys. Codeb.* 2022 (2022), p. 8. doi: [10.21468/SciPostPhysCodeb.8](https://doi.org/10.21468/SciPostPhysCodeb.8). arXiv: [2203.11601 \[hep-ph\]](https://arxiv.org/abs/2203.11601).
- [23] Jolien Cremers and Irene Klugkist. “One Direction? A Tutorial for Circular Data Analysis Using R With Examples in Cognitive Psychology”. In: *Frontiers in Psychology* 9 (2018). ISSN: 1664-1078. doi: [10.3389/fpsyg.2018.02040](https://doi.org/10.3389/fpsyg.2018.02040). URL: <https://www.frontiersin.org/journals/psychology/articles/10.3389/fpsyg.2018.02040>.
- [24] W. Cassing and E. L. Bratkovskaya. “Parton-Hadron-String Dynamics: an off-shell transport approach for relativistic energies”. In: *Nucl. Phys. A* 831 (2009), pp. 215–242. doi: [10.1016/j.nuclphysa.2009.09.007](https://doi.org/10.1016/j.nuclphysa.2009.09.007). arXiv: [0907.5331 \[nucl-th\]](https://arxiv.org/abs/0907.5331).